*The* RESEARCH LABORATORY
*of*
ELECTRONICS
*at the*
MASSACHUSETTS INSTITUTE OF TECHNOLOGY
CAMBRIDGE, MASSACHUSETTS 02139

A Touch Lab Report

# Ultrasound Backscatter Microscope for In Vivo Imaging of Human Fingertip

Balasundara I. Raju and Mandayam A. Srinivasan

RLE Technical Report No. 631

September 1999

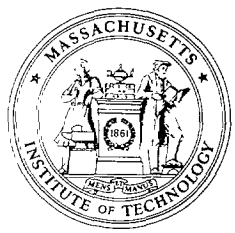

A Touch Lab Report

# Ultrasound Backscatter Microscope for In Vivo Imaging of Human Fingertip

Balasundara I. Raju and Mandayam A. Srinivasan

RLE Technical Report No. 631

September 1999

This work has been supported through NIH grant NS33778.

The Research Laboratory *of* Electronics
MASSACHUSETTS INSTITUTE OF TECHNOLOGY
CAMBRIDGE, MASSACHUSETTS 02139-4307

# Ultrasound Backscatter Microscope for *In Vivo* Imaging of Human Fingertip

by

Balasundara I. Raju

Submitted to the Department of Electrical Engineering and Computer Science
on Feb 2, 1998, in partial fulfillment of the
requirements for the degree of
Master of Science in Electrical Engineering and Computer Science

## Abstract

This thesis concerns the development of an Ultrasound Backscatter Microscope (UBM), and its application to imaging human fingertip skin under *in vivo* conditions. UBM is similar to B-mode diagnostic ultrasound imaging, but uses higher frequency acoustic waves ($\sim$ 50 MHz) to achieve resolutions of the order of tens of microns. In UBM, contrast depends on the mechanical properties of tissues, a feature which complements techniques such as optical microscopy, CT and MRI that rely on other tissue properties. UBM is less expensive than most imaging techniques, and is also non-invasive. However, because of increased attenuation of the acoustic waves at higher frequencies, tissues being imaged must be located within a few millimeters of the surface. A UBM system was designed and built using a high frequency PVDF transducer (nominal frequency of 75 MHz), a pulser, a digitizing oscilloscope, a scanning system and the IEEE488 interface. The axial and lateral resolutions were experimentally determined to be about 20 $\mu$m and 150 $\mu$m respectively.

The device was used to image human fingertip skin under *in vivo* conditions so as to obtain information about the internal structure of the finger to aid biomechanical studies of human tactile sensing. Since phased-array transducers are not available at high frequencies, echoes from tissues at different lateral locations were obtained by mechanically scanning the transducer across the finger. Signal processing was done on the reflected echoes to obtain 2-D images. Images of fingerpad skin of six human subjects showed three distinct layers up to a depth of about 1.2 mm. Comparison images of fingertip skin on the dorsal side also showed a layered structure with lesser thicknesses for the first two layers, which is consistent with known anatomical information. The thesis concludes with a discussion of possible improvements and other applications of UBM.

Thesis supervisor: Dr. Mandayam A. Srinivasan
Title: Principal Research Scientist

Thesis supervisor: Prof. Dennis M. Freeman
Title: Assistant Professor

# Contents

# List of Figures

# List of Tables

# 1 Introduction

## 1.1 Motivation

This thesis describes the development of an ultrasound backscatter microscopy system (UBM) and its application to imaging human fingertip skin. UBM is an extension of diagnostic ultrasound systems but uses higher frequency ultrasound pulses for imaging, and consequently achieves resolutions higher than diagnostic ultrasound systems. Because of the absence of superconducting magnets or radiation shields, UBM systems are less expensive and less complicated than other imaging modalities like MRI, X-ray etc. Because commercial UBM systems lack the flexibility required in a research setting, it was decided to build a system in the laboratory.

The application of UBM described in this work is human fingertip imaging under *in vivo* conditions. This work is motivated by the need to obtain anatomical information of subsurface fingertip tissues to aid biomechanical studies of human tactile sensing. The following section explains the significance of this application.

## 1.2 Human Tactile Sensing

Each of the five sensory systems in humans has unique features. The sense of touch is unique in that there is a direct interaction with the object being touched, unlike in vision, hearing, and smell, wherein the information source is located elsewhere. Certain properties of objects like mechanical compliance can be realized only through touch. Unlike in vision, hearing, or smell, during touch, one can modify the signals that are imposed on the skin by moving one's finger over the object and exploring it. A study of the human tactile system will lead to a better understanding of human interaction with surroundings and

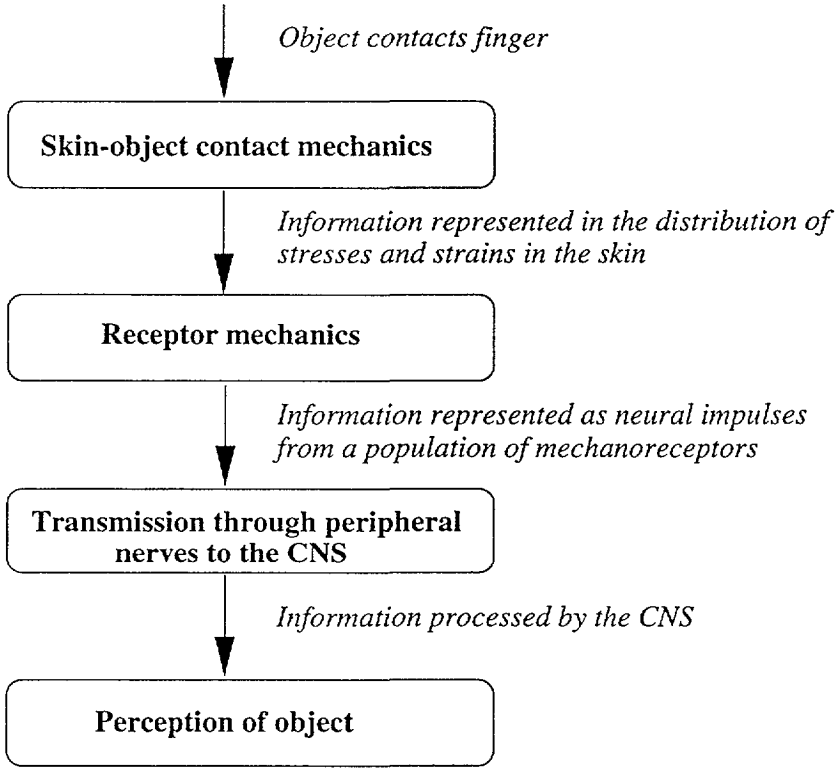


**Figure 1-1:** Sequence of events leading to tactile sensing.

will also aid engineers in the development of tactile communication aids, teleoperation systems, intelligent robots and virtual environments.

The sequence of events resulting in human tactile sense can be divided into four events for the ease of analysis: First, the object contacts the skin leading to a distribution of pressure on the skin's surface. Second, these surface pressure distributions lead to sub-surface distributions of mechanical stresses and strains, depending on the filtering properties of the skin. Third, these stresses and strains are transduced into neural impulses by the mechanoreceptors in the skin. Finally, these neural impulses reach the brain where the object is perceived. Figure 1-1 shows the above sequence of events.

Human tactile sensing has been studied mostly through neurophysiological studies (recording neural responses of peripheral nerves) or through psychophysical studies (evaluating responses of human subjects to tactile stimuli). Neurophysiological studies have

provided information on the neural behavior of the mechanoreceptors and the peripheral nerves that innervate these receptors. Psychophysical studies have yielded insights on the relationship between the stimuli applied to the skin and the overall perception of humans. However these studies alone cannot explain all the steps that take place during tactile sensing (Figure 1-1). For example, the mechanical stresses and strains in the skin, to which the mechanoreceptors respond, cannot be computed by either of the two methods. The calculation of stresses and strains requires a knowledge of the spatial distribution of tissues that make up the skin, along with their mechanical properties. This knowledge can be obtained through imaging of internal tissues in the fingertip at resolutions sufficient to reveal the underlying structures. Such information can then be used to develop finite element models to compute stresses and strains in the fingertip during tactile sensing, and the relationship between these stresses and experimentally recorded neural responses can be studied. It is expected that such studies, in the long term, will lead to a better understanding of the human tactile system and will also aid in the development of intelligent prosthetic limbs, anthropomorphic robots, and virtual environments for training and teleoperation.

## 1.3 Thesis Overview

This thesis describes the development of the ultrasound backscatter microscope and its usage in obtaining fingertip images. Chapter 2 provides background information on the anatomy of the human fingertip, summarizes the previous work in human tactile sensing, explains the need and the requirements of the fingertip images, and also provides background information on various imaging modalities. The reason for choosing ultrasound backscatter microscopy is described in detail.

Chapter 3 provides a description of the working of ultrasound backscatter microscopy. Thereotical information on factors limiting image resolution and depth of imaging is provided. The design of the overall system and the requirements placed on the various subsystems is presented.

Chapter 4 describes the processing of raw signals to obtain images. The experimental

determination of axial and lateral resolution is described. Images of graphite-gel phantoms are also discussed.

Preliminary fingertip images are discussed in Chapter 5. Possible anatomical correlations are provided. This chapter also describes image processing steps required for displaying the images.

Chapter 6 summarizes the significance of the present work and its application to human tactile sensing. Other possible applications of UBM are presented. Possible improvements in the design of the system are also suggested.

# 2 Background

## 2.1 Anatomy of the Human Fingertip

The human fingertip is a complex organ. The major structural components that make up the fingertip are the skin, subcutaneous tissues mostly composed of fat, bone and nail. Figure 2-1 (a) shows a cross-sectional view of a human fingertip. A typical human fingerpad is about 10 to 20 mm in diameter and the length of the distal phalanx (endmost bone) varies between 20 to 30 mm. The skin on the palmar side is thick compared to most parts of the body and is used for grasping as well as fulfilling sensory functions. The palmar skin is also characterized by the presence of finger prints. The following subsection contains a detailed anatomical description of the fingertip skin, which will provide material for discussion of fingertip images in Chapter 5.

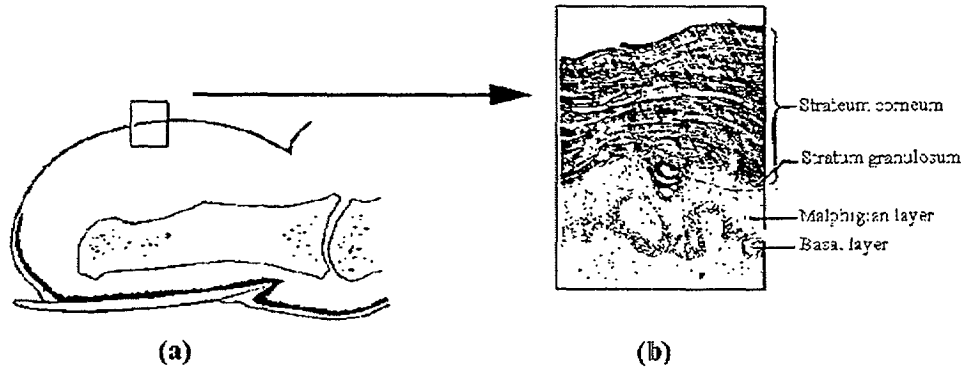


**Figure 2-1:** (a) Cross-section through a finger (adapted from O'Rahilly (1969)). (b) Different layers in the epidermis (adapted from Thomine (1981)).

### 2.1.1 Fingertip Skin

The fingertip skin can be subdivided into an outer layer called epidermis, and an inner layer called dermis. The epidermis, in turn, is made up of five layers as shown in Figure 2-1 (b). The topmost layer is the *stratum corneum* which consists of dead keratinized cells with no detectable intercellular spaces. This layer is considered water-proof (Lockhart *et al.* , 1965). The next layer is the *stratum lucidum* which contains cells that have apparently lost their nuclei and cell boundaries. It is typically present only in the palmar or plantar skin and is about two or three cells thick. The third layer is the *stratum granulosum* which contains granules produced during chemical changes occurring within cells as they progress to the topmost layer. This layer is also about two to three cells thick. The fourth layer is the *malphigian layer* which consists of a thick, multicellular layer of polygonal cells which get flatter as they approach the surface. This layer is the site of cellular multiplication and plays a significant part in skin regeneration. The bottom most layer is the *stratum basale,* which is separated from the bottom dermis by a fine acellular structure called the basement membrane. The stratum basale is attached to the basement membrane by means of protoplasmic prolongations known as hemidesmosomes. The dermis is attached to the basement membrane by collagen or retinacular fibrils, which thus indirectly fasten the dermis to the epidermis. The epidermis and dermis are separated by internal ridges called intermediate and limiting ridges.

The dermis consists of a superficial *papillary layer* and a deeper *reticular layer,* and is made up of collagen fibers, elastin fibers, blood vessels and nerve endings. The papillary layer is a close knit network of fibrous and elastic tissue. The reticular layer contains thicker collagen fibers than the papillary layer, and has numerous elastin fibers that run mostly parallel to the skin's surface.

The surface of the finger is characterized by the presence of ridges. The direction of these ridges reflect that of the underlying internal ridges. Also most of the epidermal and dermal layers run parallel to these ridges. The spacing between the ridges is about 500 $\mu$m.

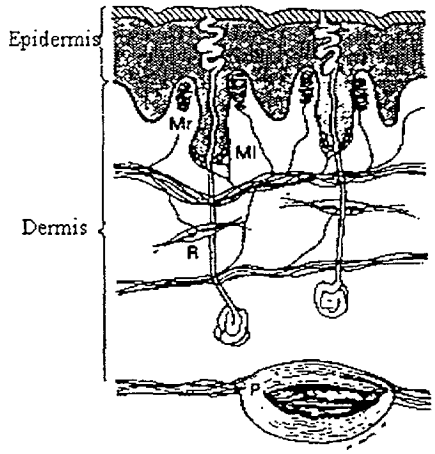


**Figure 2-2:** Cross-section through a fingertip skin showing the four mechanoreceptors (adapted from Johansson and Vallbo (1983)): Mr - Meissner's Corpuscles; MI - Merkel Discs; R - Ruffini Corpuscles and P - Pacinian Corpuscles. The figure is not drawn to scale.

### 2.1.2 Mechanoreceptors

The human fingertip skin is innervated by a variety of peripheral afferent nerve fibers. The receptors at the end of the nerves can be classified broadly as mechanoreceptors, thermal receptors and nociceptors (pain receptors). Among the mechanoreceptors in the human fingertip skin, four types have been identified and their locations are shown in Figure 2-2. These are the Meissner's Corpuscles, Merkel Discs, Ruffini Corpuscles and Pacinian Corpuscles. These four mechanoreceptors vary in their size, location and neural behavior. Table 2.1 summarizes some of the properties of these mechanoreceptors.

The nerve fibers innervating the mechanoreceptors have been classified primarily based on their adaptive properties in response to time-varying indentation on the most sensitive part of the fiber's receptive field. A "ramp and hold indentation" as shown in Figure 2-3 is applied to the finger and responses of the corresponding peripheral afferents are recorded. Two of the afferents respond only to the ramp (dynamic) phase of the stimulus and are referred to as the Rapidly Adapting (RA) and the Pacinian (PC) afferents. The other two afferents respond to both the ramp (dynamic) as well as the hold (static) phase of the stimulus and are referred to as the Slowly Adapting Type-I (SA-I) and Slowly Adapting

| | Merkel | Ruffini | Meissner | Pacini |
|---|---|---|---|---|
| Location | Basal layer cells of the epithelial glandular ridges | Dermis | Dermal papillae protruding upward into the epidermis | Deeper layers of dermis, subcutaneous fat |
| Depth | 0.7–1.0 mm | 0.8-1.5 mm | 0.5–0.7 mm | 1.5 –2.0 mm |
| Size | 10 $\mu$m | 500 – 1000 $\mu$m long, 200 $\mu$m in central zone and 30-40 $\mu$m diameter near the poles | 100 × 50 $\mu$m | long axis 0.3 – 1.5 mm, diameter 0.2 – 0.7 mm |
| Shape | Oval or rounded | Ellipsoidal | Ellipsoidal | Ovoid |
| Morphological Classification | Un-encapsulated, Epidermal | Encapsulated, Dermal | Encapsulated, Dermal | Encapsulated, Dermal |
| Structure | Groups of 5–10 cells at a site | 4–5 layers of lamellar cells covered by a basement membrane | Each fiber has a irregular discoidal form oriented at right angles to the long axis of the corpuscle | Several layers of concentrically packed lamellar cells, subcapsular space filled with fluid |
| Sensitivity to Stimuli | displacement and velocity | displacement and velocity | velocity | velocity |
| Innervating Afferent Fiber | Slowly Adapting type I (SA-I) | Slowly Adapting type II (SA-II) | Rapidly Adapting (RA) | Pacinian (PC) |

**Table 2.1:** Comparison of four mechanoreceptors found in the primate fingerpad. Adapted from Dandekar and Srinivasan (1995).

Type-II (SA-II) afferents. From Table 2.1 it can be seen that all the mechanoreceptors are located within the top 2 mm of the skin's surface. This information is useful in determining the depth of imaging for the imaging system.

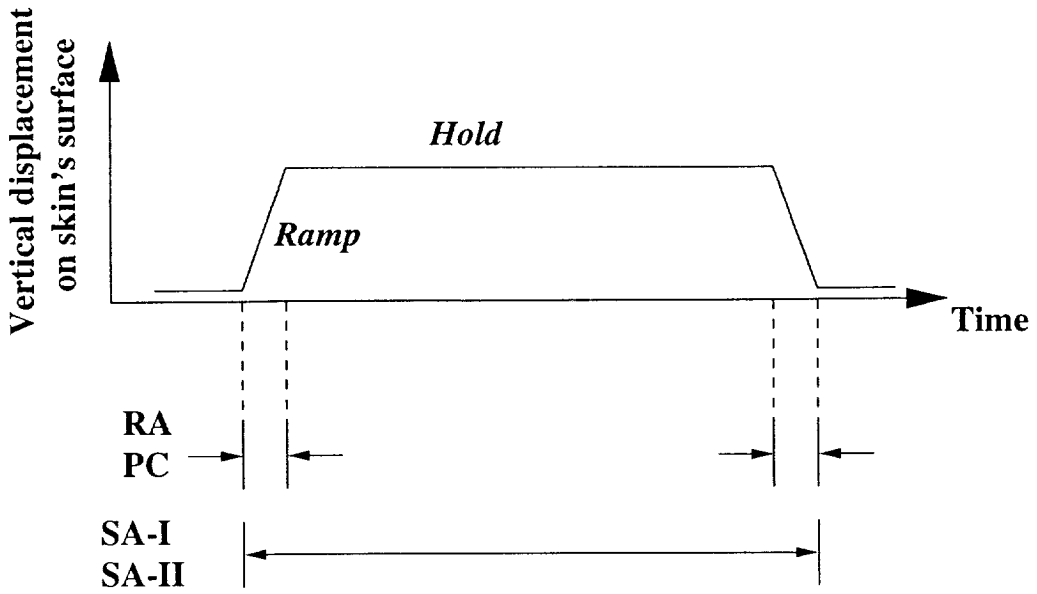


Figure 2-3: The four afferent nerve fibers innervating the mechanoreceptors are classified based on their response to time-varying stimuli such as the one shown. The RA and PC afferents respond only to dynamic stimuli while the SA-I and SA-II afferents respond to both dynamic as well as static stimuli.

## 2.2 Previous Studies in Human Tactile Sensing

This section summarizes some of the salient works in the field of human tactile sensing. The work done in human tactile sensing can be categorized into three distinct areas: neurophysiology, biomechanics and psychophysics.

### 2.2.1 Neurophysiological Studies

Neurophysiological studies in tactile sensing have involved applying a known object to the fingertip of a monkey or human, recording the peripheral neural responses, and analyzing the data to infer the neural behavior of the mechanoreceptors. These works include the study of neural behavior of the mechanoreceptors such as the mechanical-to-electrical transduction mechanism, size of receptive fields, sensitivity, threshold, and innervation density. Mountcastle and co-workers studied extensively the relation between neural response and perception (Mountcastle and Powell, 1959; Mountcastle *et al.* , 1972). Loewenstein and Skalak (1966) studied the mechanical-to-electrical transduction in the pacinian corpuscle. Knibestol and Vallbo (1970) established that there are at least four classes

of cutaneous mechanoreceptors in the human fingertip. Knibestol (1973; 1975) studied the stimulus-response functions of slowly and rapidly adapting afferents and developed mathematical models for the discharge rate as functions of stimulus intensity. Johansson (1978), and Johansson and Vallbo (1979) studied the receptive field characteristics of the human mechanoreceptors and their innervation densities. These, and other works are well reviewed in Darian-Smith (1984), and Johansson and Vallbo (1983). Later studies have also focussed on the relationship between the properties of the object contacting the fingertip such as its shape, compliance etc., and the responses of the afferent nerve fibers. Phillips and Johnson (1981a) indented monkey fingerpads with rectangular bar shapes and recorded the afferent neural responses. Srinivasan and LaMotte (1987) indented sinusoidal step shapes to monkey fingerpads and recorded the afferent neural responses under both static and dynamic conditions. These works led to hypothesis that the geometrical feature of the object that is encoded by the afferent responses is its curvature (LaMotte and Srinivasan, 1993). To summarize, neurophysiological studies utilized peripheral neural recordings to learn about the neurophysiological properties of the afferents, as well as the relationship between the responses and properties of the objects indenting the fingerpad.

### 2.2.2 Psychophysical Studies

Psychophysics is concerned with the quantitative relationship between physical stimuli and the resulting behavioral responses of human subjects under carefully designed test conditions. Unlike neurophysiology, psychophysics studies the overall behavior of the tactile system including the final subjective perception. Some specific earlier works in this area include the study of vibrotactile perception (Verillo *et al.*, 1969), roughness perception (Lederman and Taylor, 1972), spatial resolution (Lederman and Taylor, 1972; Loomis, 1979), and texture discrimination (Lamb, 1983) during touch. Though psychophysical studies were initially done independently, later they were often combined with neurophysiological studies in order to relate the peripheral neural responses to perception (Talbot *et al.*, 1968). A good review of earlier psychophysical research in tactile sensing is presented in Loomis and Lederman (1986). Later efforts have involved tactile discrimination of curvature (Goodwin *et al.*, 1991), tactile discrimination of softness (Srinivasan and LaMotte, 1995) and tactile discrimination of thickness (Ho and Srinivasan, 1996). Psychophysical evidence that four "channels" participate in perception was presented by Bolanowski *et. al.* (1988).

These four channels are believed to have unique properties with regard to their frequency response, threshold, temperature dependence, etc. To summarize, psychophysics utilized subjective human perception to study the overall mechanism of touch.

### 2.2.3 Biomechanical Studies

The biomechanical approach to tactile sensing focusses on the mechanical aspects of touch including determination of mechanical properties of skin and other fingertip tissues, mechanistic modeling of the fingerpad, computation of stress-strain measures in the vicinity of the mechanoreceptors, and a study of the relationship between these stress-strain measures and recorded peripheral neural responses. The study of mechanical properties of the skin in general also contributed to the effort in this direction. For example, the mechanical properties of the skin were found to be strongly dependent on species, age, sex, exposure and hydration (Tregear, 1966; Lanir, 1987), which implies that *in vitro* measurements of the mechanical properties of the skin could vary considerably. Skin has also been found to exhibit viscoelastic behavior and has rate-dependent stress-strain relations (Fung, 1981). Phillips and Johnson (1981b) in their study of relationship between subsurface strain measures and recorded neural impulses, modeled the finger as an infinite, isotropic, linear elastic, homogeneous medium, and found that maximum compressive strain measured at a depth of 0.75 mm was the best mechanical measure that could be linearly related to SA-I afferent responses. Srinivasan (1989) modeled the finger as an incompressible fluid enclosed by an elastic membrane and was able to predict the experimentally measured deformations on the surface of the finger. Gulati and Srinivasan (1996) indented human fingers with shaped objects, measured the temporal force responses and proposed a non-linear Kelvin type model to describe the overall mechanical behavior of the fingerpad. Dandekar and Srinivasan (1996) developed two dimensional and three dimensional finite element models of primate fingertips in order to relate subsurface strain measures to recorded neural responses of SA-I afferents. Maximum compressive strain and strain energy density were found to be the best candidates that could be linearly related to the responses of SA-I afferents. To summarize, the biomechanical studies have aided the neurophysiological studies in relating the mechanical quantities such as stress and strain to recorded neural responses.

## 2.3 Need for Imaging the Human Fingertip

While the neurophysiological and psychophysical approaches have been used in tactile sensing for a long time and have yielded useful insights, the biomechanical approach has been of interest only recently, primarily because of the following limitations:

- The non-availability of *in vivo* material properties of tissues
- Absence of knowledge of internal geometry of fingerpad, especially with regard to "mechanical boundaries" - boundaries where mechanical properties change
- Limited experimental techniques to observe internal tissue deformations, under *in vivo* conditions

The mechanistic aspects of touch, especially the computation of stress-strain measures in the vicinity of the mechanoreceptors is of primary importance in the study of tactile sensing as it determines the magnitude and distribution of the mechanical stimulus, or "input", to which the afferent nerve fibers respond (Raju, 1998). In order to aid biomechanical studies, three dimensional finite element models of primate fingertips were developed (Dandekar and Srinivasan, 1996; Raju, 1998). While these models maintain realistic external geometry of the fingertip, the internal geometry, e.g., the structure of the epidermal and dermal ridges, is idealized. Imaging the internal structure of the fingerpad will help to refine these models by incorporating internal tissue geometry. Imaging of fingertip has other advantages: By comparing images taken before and after the application of a known load to the finger, the displacements of the internal tissues, and consequently the internal strain distributions, can be obtained. Such a procedure will obviate the use of time-consuming computer simulations in future. Additionally, imaging can also be used to obtain the Young's modulus distribution within tissues (Cohn *et al.* , 1997a). This will help to obtain mechanical properties of the fingertip tissues under *in vivo* conditions.

With high resolution imaging and sufficient contrast, it might also be possible to image directly the mechanoreceptors and their deformations during touch. Such a study, if possible, will then open an entirely new way of studying tactile sensing, in addition to the neurophysiological, psychological and biomechanical methods already being used.

## 2.4 Imaging Requirements

Before choosing an imaging technique (or developing ones's own technique) for fingertip imaging, the requirements expected from the images must be clearly identified. First, in order to observe internal tissue deformations during touch, the imaging must be capable of being done under *in vivo* conditions. Second, since most of the mechanoreceptors are located inside the skin within a depth of 2 mm from the surface, the imaging technique must be able to image tissues up to a depth of about 2 mm or more. Third, since the features of the skin are small (e.g., the wavelength of the finger prints is about half a mm) resolutions about 10 times that of the wavelength of the finger prints, i.e., 50 $\mu$m is needed. Fourth, in order to identify distinct layers in the skin, the technique should have good material contrast. Also, since the images will be used to aid biomechanical studies of touch, a technique in which the contrast depends on the mechanical properties of the tissues would be preferred. Fifth, in order to minimize motion artifacts during imaging, the time of imaging should be minimized. Otherwise any effort to obtain good resolution will be offset by gross motions due to the restlessness and involuntary movements of the subject's finger. Finally, since the imaging is done on human subjects, the technique should be non-invasive.

## 2.5 Overview of Imaging Modalities

There are several imaging modalities available today. Most *in vitro* techniques like scanning electron microscopy provide high resolution and have been used in imaging thin slices of biological tissues. However the requirement of vacuum, and the requirement of staining makes them unsuitable for the present purpose. Also most *in vitro* techniques like scanning acoustic microscopy and confocal microscopy can image only surface or near-surface tissues (up to a depth of about 100 $\mu$m). Currently the modalities for *in vivo* imaging include computed tomography (CT), diagnostic ultrasound, magnetic resonance imaging (MRI), single-photon emission computed tomography (SPECT), positron emission tomography (PET), and optical coherence tomography (OCT). These modalities vary greatly in their application and capability. The properties of these modalities are summarized in Tables 2.2 and 2.3. It can be seen that CT does not provide sufficient resolution for the present work. MRI also has limited resolution, though advances in technology could

yield higher resolutions in future (Zhou and Johnson, 1995). Diagnostic ultrasound has good penetration and contrast, but has poor resolution. SPECT and PET belong to the family of nuclear medicine and are used for obtaining functional data such as the presence of tumor, metabolic functions etc. They are not used for anatomical imaging. OCT is a recently developed technique that has high resolution especially for eye and vascular imaging (Huang *et al.* , 1991; Brezinski *et al.* , 1996). However because of very limited penetration, and because of the dependence of contrast on the optical properties of tissues, the technique is less suited for skin imaging. Thus, there is no one technique that is readily available for the current purpose.

## 2.6 Previous work in Imaging the Fingertip

Currently very few efforts have been taken towards human fingerpad imaging under *in vivo* conditions, especially for biomechanical applications. The only previous work in this direction was the utilization of MRI (Voss and Srinivasan, 1998). Using a 4.7 Tesla system, fingerpad images were obtained when the finger was left free, as well as when the finger was indented with objects of known geometry. MRI was shown to be able to image the entire cross-section of the finger, including the bone. The images had a theoretical resolution of 125 $\mu$m by 125 $\mu$m. The actual resolution was poorer because the thickness of the slice being imaged was 500 $\mu$m. The images provided good contrast between skin, fat, and bone, but missed the finger prints on the surface of the finger, probably due to lack of moisture and averaging in the thickness direction. The technique proved useful to obtain overall macroscopic details of internal tissue geometry, but did not prove useful to obtain microscopic details of the internal tissues.

## 2.7 Ultrasound Backscatter Microscope

None of the current imaging modalities, without modifications, are directly applicable for the current work. Of the broad classes of imaging (optical, acoustic, MRI etc.), acoustic imaging is the best choice at the moment, primarily because of the direct relationship of contrast to mechanical properties of the tissues. Though ultrasound by itself does not have sufficient resolution, recent and ongoing developments in ultrasound transducer designs

| Modality | Principle | Diagnostics | Contrast Mechanism | Cost |
|---|---|---|---|---|
| CT | X-rays | Anatomical | Density distributions. Poor for differentiating between soft tissues. | Medium cost ($\approx$ \$250,000) |
| MRI | Nuclear magnetism | Anatomical and functional | Spin-lattice ($T_1$) and Spin-spin ($T_2$) relaxation constants. Good soft tissue contrast. | Expensive (requires superconducting magnets $\approx$ \$2.5 million) |
| Diagnostic Ultrasound | Acoustic waves | Anatomical | Discontinuities in density and young's modulus. Good for differentiating most tissue boundaries. | Low cost (\$100,000) |
| SPECT | Isotope emissions | Functional | Photon emission from ingested isotopes | Medium cost |
| PET | Isotope emissions | Functional (*in vivo* physiologic and metabolic functions) | Affinity of tissue to ingested positron emitting isotopes | Expensive (requires a particle accelerator) |
| OCT | Low-coherence interferometry | Anatomical | Optical reflections from tissues. Good for eye imaging but less suited for skin imaging. | |

**Table 2.2:** Comparsion of various imaging modalities.

| Modality | Depth of Imaging | Resolution | Duration | Invasiveness |
|---|---|---|---|---|
| CT | > 10 cm | 0.25 mm | 20 minutes for volume data | Medium |
| MRI | Full penetration possible | 0.125 mm | 20 - 40 minutes for volume data | Small |
| Diagnostic Ultrasound | 10 cm | 1 mm | 1 - 2 minutes for sectional data | Negligible |
| SPECT | | | | High |
| PET | | | | High |
| OCT | $\approx$ 1mm | 0.02 mm | 1 - 2 minutes | Low |

**Table 2.3:** Comparsion of various imaging modalities. The numerical values in the table are approximate values. SPECT and PET are used for functional imaging and not anatomical imaging. Hence some of their columns are left blank.

have led to a new technique called ultrasound backscatter microscopy (UBM) (Foster *et al.* , 1993). UBM is similar to conventional ultrasound B-mode imaging, but uses higher frequency, focussed, and short-pulsed sound waves (> 20 MHz) for imaging. Because of increased attenuation of acoustic waves at higher frequencies, UBM sacrifices penetration depth to attain increased resolution. Typically penetration depths up to 1 to 2 mm have been reported with resolutions between 20 to 100 $\mu$m, the exact values depending on the transducer characteristics. Since non-ionizing (acoustic) waves are used, the technique is non-invasive. The imaging time which depends on the extent of imaging, can be as low as half a minute for a 2 mm scan [1].

Currently, UBM has been used mostly for the detection of tumors and lesions. Areas of *in vivo* imaging include eye (Foster *et al.* , 1990), and skin (Passmann and Ermert, 1996; Turnbull *et al.* , 1993). *In vitro* imaging of gastrointestinal walls have also been reported (Wiersema *et al.* , 1989). Recently the technique has also been used as an elasticity microscope, wherein the elasticity distributions in tissue mimicking phantoms can be computed (O'Donnell *et al.* , 1994; Cohn *et al.* , 1997a; Cohn *et al.* , 1997b). Currently commercial UBM systems are very limited and do not offer the flexibility required in a research work

[1] With motorized, computer-controlled scanning systems.

for a new application. Hence it was decided to develop a system in the laboratory.

# 3 Ultrasound Backscatter Microscope

This chapter explains the general principles, features, and the design of the ultrasound backscatter microscope used in this work.

## 3.1 Ultrasound

Ultrasound is a well known medical diagnostic tool (Devey and Wells, 1978; Kremkau, 1993; Shung *et al.* , 1992). Ultrasound uses sound waves having frequency higher than 20 kHz, the upper limit of human audible range. The need for using ultrasound rather than audible sound is that the wavelength of the wave, and hence the resolution of the image, is inversely related to the frequency of the wave. Audible sound has a wavelength on the order of half a meter and is therefore not useful for diagnostic imaging. Ultrasound waves on the other hand have much smaller wavelengths. When sound waves are propagated through a human tissue, they are reflected and scattered by the tissue. These reflected signals are then analyzed to obtain information about the tissue. In conventional diagnostic ultrasound imaging, sound waves in the frequency range 1 to 10 MHz are commonly used. Anatomical information with a resolution of about 1 mm can be obtained from tissues lying as deep as 10 cm. Common applications include echoencephalography, opthalmology, obstetrics, and doppler vascular imaging.

Another imaging technique that uses ultrasound waves at much higher frequencies is scanning acoustic microscopy (Lemons and Quate, 1979; Briggs, 1992). The primary difference between diagnostic ultrasound and scanning acoustic microscopy (SAM) is that whereas ultrasound uses relatively low frequency waves (1 to 10 MHz), scanning acoustic microscopy uses higher frequency waves (500 MHz or higher). While diagnostic ultrasound produces low resolution images of deep tissues, SAM produces high resolution

microscopic images of surface tissues, usually *in vitro*. Typical applications of SAM are imaging thin slices of tissue (few microns thick) and imaging flaws in microelectronic circuits. Moreover SAM is commonly used in transmission imaging mode with separate transducers for transmission and receiving, whereas diagnostic ultrasound is always used in reflective (or backscatter) mode with the same transducer used for both transmission and receiving. Under certain conditions, SAM can achieve resolutions better than those achievable using scanning electron microscope, and also with better image contrast (Briggs, 1992).

## 3.2 Ultrasound Backscatter Microscopy

Neither diagnostic ultrasound nor SAM are useful for high resolution *in vivo* imaging. However, by using frequencies between those used in diagnostic ultrasound and SAM, it might be possible to achieve a trade off between resolution and depth of imaging. This idea led to the development of a third imaging technique that uses acoustic waves in the frequency range 20 to 150 MHz, and has been named as ultrasound backscatter microscopy (UBM) in order to distinguish it from both diagnostic ultrasound and SAM (Foster *et al.*, 1993). UBM is still in development and few commercial systems exist.

Though UBM is similar to both diagnostic ultrasound and SAM, there is one important difference, other than the imaging frequency. In SAM, imaging resolution is high only in the lateral direction (perpendicular to the direction of the wave). The axial resolution (along the direction of the wave) depends, in addition to the frequency, on the bandwidth of the transducer used. As SAM is used for surface imaging (lateral imaging), there are no requirements on the bandwidth of the transducer used. In diagnostic ultrasound, the axial resolution is poor and again there is no bandwidth requirement on the transducer. In UBM, the bandwidth of the transducer has to be high in order to achieve good axial resolution. The development of sensitive transducers with sufficient bandwidth (made of polymer or ceramic) was achieved only recently (Foster, 1995).

## 3.3 Overall Working of UBM

Figure 3-1 shows a block diagram of a laboratory setup of UBM. The system consists of a transducer which is a piezoelectric material that generates sound waves when excited by a high voltage from a pulser. These sound waves are focussed towards the tissue being imaged. The tissue is submerged under water, as the acoustic impedance of the transducer matches that of water, thus eliminating any unwanted reflections as the wave leaves the transducer. The waves are reflected from several depths from within the tissue. The same transducer converts the reflected echoes back to electrical signals. These signals are then sent to a receiver unit which is also housed inside the pulser unit. The receiving electronics consists of a bandpass filter whose upper and lower frequency cutoffs can be varied, an attenuator, and an amplifier whose gain ratios can be varied so as to fit the voltage range of the digitizer. The digitizer samples the acquired waveforms at high speed which are then sent to a PC through an IEEE488 interface. After obtaining the reflected echoes at one location, the transducer is moved laterally and the process is repeated. The raw data are sent to a Unix workstation and processed to obtain an image of the tissue. The "1-D image" at any given location of the transducer is commonly referred to as an A-scan (tissue information is contained in the *amplitude* of the signal) and the complete 2-D image after processing is referred to as a B-scan (in diagnostic ultrasound, different tissues are displayed with different *brightness* levels on a CRT).

## 3.4 Contrast Mechanisms

This section describes the mechanisms that leads to tissue contrast in ultrasound. These mechanisms are common to diagnostic ultrasound, SAM and UBM. The usefulness of ultrasound as an imaging tool is primarily the result of reflection and scattering at tissue boundaries. Whenever a wave passes from a region of one value of acoustic impedance to a neighboring region of different impedance, a certain amount of incident power is reflected at the boundary and the remainder continues as a transmitted wave. The reflected wave serves as an indicator of the type of tissue at the boundary, whereas the transmitted wave probes deeper interfaces. The reflection coefficient when a wave makes a normal incidence (i.e., when a plane wave is incident on a parallel plane boundary) is given by the following

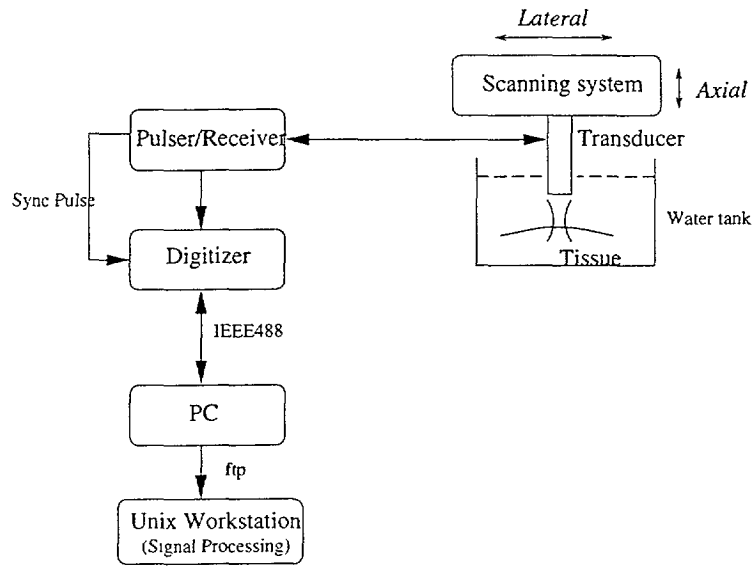


**Figure 3-1:** Block diagram of a UBM setup.

expression:

$$R = (\frac{Z_2 - Z_1}{Z_2 + Z_1})^2 \tag{3.1}$$

where $Z_1$ and $Z_2$ are the acoustic impedances of the first and second media. For example, if the tissue being imaged is perfectly homogeneous, then the wave traveling through it will see no difference in impedance and hence there will be no reflection. The acoustic impedance of a medium is the product of the velocity of sound in that medium and its density (Christensen, 1988):

$$Z = \rho v \tag{3.2}$$

where $\rho$ is the density of the medium and $v$ is the velocity of the wave in that medium. The velocity of the wave in turn depends on the stiffness and density of the medium. In biological tissues the acoustic waves are mostly longitudinal waves and the velocity is given by:

$$v = \sqrt{\frac{E}{\rho}} \tag{3.3}$$

where E is the Young's Modulus of the medium. Thus, the impedance of the medium is determined by its mechanical properties, namely Young's Modulus and density. Thus

contrast in ultrasound imaging depends on the differences of the mechanical properties between adjacent tissues.

The incident waves undergo perfect reflection only if the tissue boundaries are smooth and if the wavelength is small compared to the boundary dimensions. If on the other hand, the boundary dimensions are comparable to the wavelength, or if the boundary is not smooth, the phenomenon that occurs at the boundary is scattering. Scattering is the redirection of the incident wave in all directions. Contrast due to scattered waves is still dependent on impedance mismatch. However because the incident wave is spread out in several directions, the intensity of the wave scattered back towards the transducer ("backscattered wave") is much less than that of a wave that is reflected from a smooth surface. This problem is overcome by using highly sensitive transducers. Despite the reduction in intensity, scattering provides an important advantage over reflection. In reflection, the intensity of the wave is highly dependent on the angle of incidence. If the surface is tilted even slightly, the transducer will not receive any of the reflected signal. However, scattering makes echo reception from tissues less dependent on the incident angle. Since most tissues in the human body are considered rough (Kremkau, 1993), it is the intensity of scattered waves rather than the intensity of reflected waves that provides tissue contrast.

## 3.5 Transducer Characteristics

The characteristics of the imaging system such as the resolution and imaging depth are dependent on the transducer used. There are three parameters that determine the resolution of the image: center frequency, bandwidth and the f-number of the transducer.

*Axial Resolution:* Axial information is obtained by analyzing the time of arrival of echo signals. Therefore, axial resolution is limited by the temporal response properties of the transducer: images will be "blurred" in the axial direction if the ultrasound pulse is long. The transducer is a resonant system, and the shortest pulse is determined by the impulse response of that resonant system. Assuming that the resonance can be characterized by a quality factor $Q$, which is the ratio of the center frequency $\nu$ to bandwidth BW, the width

of the impulse response $T$ can be approximated as

$$T = \frac{1}{BW} \tag{3.4}$$

The axial blurring will then be on the order of $\delta Z$ where

$$\delta Z = cT/2 \approx c/(2BW) \tag{3.5}$$

where $c$ is the speed of propagation of the acoustic wave and the factor of 2 results because the wave traverses the same path twice: once from transducer to target and once in reverse. Thus it can be seen that, for a given propagation velocity, the bandwidth of the transducer determines the axial resolution.

*Lateral Resolution:* The lateral resolution is limited by diffraction effects. The lateral resolution is typically taken to be the (full) width of the beam where the intensity falls to half its maximum value (Briggs, 1992):

$$\delta x = (\text{f\_number})\lambda = (\text{f\_number})c/\nu \tag{3.6}$$

where f_number is the ratio of the focal length to diameter of the transducer and $\lambda$ is the wavelength corresponding to the center frequency of the transducer.

*Depth of Imaging:* All tissues attenuate acoustic waves and the attenuation increases with increasing frequency (Hill, 1986). The imaging depth characterizes how deep the echoes travel before losing amplitude to an extent that they cannot be distinguished from noise. For soft tissues this is approximately 0.5 dB/cm/MHz$^{1.2}$ (Kremkau, 1993). For example at 75 MHz, the signal loss is about 90 dB/cm. If a dynamic range of 45 dB is available, the imaging depth is 0.5 cm.

Figure 3-2 shows a graphical illustration of the image resolution and depth of imaging.

*Depth of Focus:* The transverse size of the beam is smallest at the focus, but increases as we move away from the focus. The axial distance over which the beam maintains its

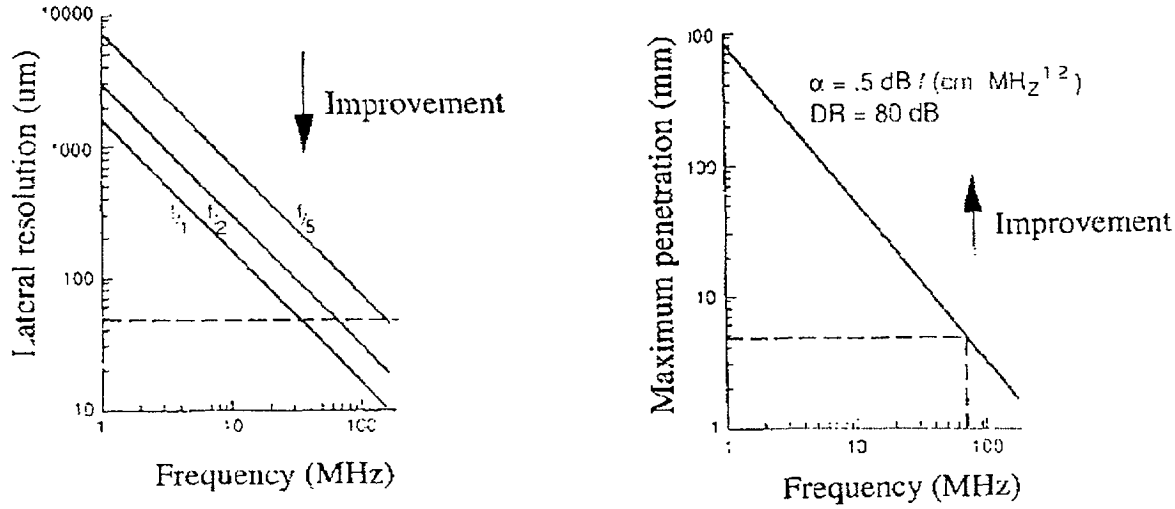


**Figure 3-2:** Lateral resolution vs depth of imaging. Smaller features can be resolved with increasing frequency and smaller f-numbers. However the depth of imaging decreases with increasing frequency because of attenuation. Figure adapted from Foster *et. al.* (1993).

approximate focussed size is termed as the depth of focus. This can be calculated based on the f-number and wavelength as (Christensen, 1988):

$$\text{DOF} = 3(\text{f\_number})^2\lambda \tag{3.7}$$

Thus improving lateral resolution using smaller f-numbers leads to smaller depth of focus. Having a smaller depth of focus could be undesirable because the lateral resolution becomes poorer as we move away from the focus. However this does not pose a serious limitation because multiple-depth-of-focus techniques can be used (Passmann and Ermert, 1996; Cohn *et al.* , 1997a). The transducer can be moved towards or away from the tissue, thereby changing the location of the focus region. Scans from these different axial locations of the transducer can be combined so as to provide a composite image, with each sub-image taken at different depths [1].

*Choice of transducer:* Apart from the above parameters, the choice of the transducer depends

[1] In the current system, this technique was not needed.

on other factors. These include physical size, presence/absence of delay line noise, availability and cost. Initially three quartz transducers with frequencies 75, 90 and 100 MHz were tried. Most quartz transducers have fused silica material to match their impedance with that of water. The presence of fused silica produced echoes that interfered with the echoes from the tissue and hence quartz transducers were not pursued. Polymer transducers made of Polyvinylidene Diflouride (PVDF) do not have this problem, as their impedance is better matched with that of water. Polymer transducers also have wide bandwidth and high sensitivity making them more suitable for the current application. The use of PVDF for external applications such as eye and skin imaging [2], has been reported (Sherar and Foster, 1987b; Sherar and Foster, 1989a). Since the technology to produce these transducers was developed recently, these transducers are not mass produced. At present there are very few companies that supply transducers at these frequencies. A transducer with a nominal frequency of 75 MHz and a bandwidth of 43 MHz and an f-number of 4 made by Panametrics (model PI-75) was chosen. This transducer was the only readily available one for frequencies greater than 50 MHz.

## 3.6 Pulser/Receiver

The pulser should be able to provide repeated pulses to excite the transducer at high pulse repetition frequencies (PRFs). The excitation pulse is a short square wave that has a wide bandwidth. The rise time of the pulse should be small enough to have sufficient energy at the center frequency of the transducer. The Panametrics pulser (model PR8900) was chosen for this purpose. This pulser has can go up to PRFs of 20 kHz. It has a rise of time of less than 1 $ns$. The pulser unit also contains the receiving electronics. The receiver processes the signals from the transducer before sending the signals to the digitizer. The processing steps include bandpass filtering to reduce noise, amplification, and attenuation so as to match the input range of the digitizer. The unit can also be controlled using a GPIB (General Purpose Interface Bus) interface from a PC.

[2] For intravascular imaging, ceramic transducers, which are smaller in size, are used.

## 3.7 Data Acquisition

The data acquisition system digitizes the analog waveforms from the receiver and sends them to a computer. There are several requirements for the data acquisition system. These include sufficient bandwidth, high sampling rate, sufficient memory, minimal dead-time between acquisitions, windowing capability, averaging capability, fast data transfer rate to a PC and automated control from the PC. A Tektronix digitizing oscilloscope TDS520C was chosen for this purpose. The scope has a bandwidth of 500 MHz which is higher than the bandwidth of the reflected echoes (about 100 MHz). Sampling rates as high as 500 MS/s (million samples per second), for dual channel operation, can be chosen. This is five times the signal bandwidth and thus provides more-than-twice-oversampling. The scope also has windowing capability, which is a very useful feature as typically the useful signal is present only within a small time window of an entire acquisition. Windowing only the needed portion greatly reduces the required memory length (and cost) to store an acquisition. The scope can successively acquire multiple acquisitions with only a dead-time of 20 $\mu$s, which is smaller than the pulse repetition period of 100 $\mu$s. The scope has a memory of 130K samples per channel which is sufficient to store one hundred acquisitions if each acquisition contains 1000 points. The scope can average multiple acquisitions in real-time, a feature which is very important in tissue characterization studies. Also one can selectively transfer only the averaged waveform to the PC. This feature reduces the total time of data transfer, and hence the total time for imaging. All the controls on the scope can be controlled by a PC through the GPIB interface. A simple C program is all that is required to automate the data acquisition process.

## 3.8 Scanning System

The transducers used for UBM are single-element transducers unlike the phased-array transducers used in diagnostic ultrasound. Thus the transducer has to be moved mechanically to obtain echoes from different lateral locations. There are several requirements for the scanning system. The scanning system should be able to move the transducer in at least two directions — horizontally for lateral positioning, and vertically for multiple-depth-of-focus imaging. Additionally a third degree of freedom — to rotate the transducer to image curved portions of the finger — will be useful. The system should have high accuracy

and repeatability. It should also have sufficient travel length so that the transducer can be easily positioned with respect to the finger. In order to achieve these requirements, and to reduce the overall costs of the system, a manual positioning system from Parker-Hannafin was chosen. The positioning system has three degrees of freedom (vertical, horizontal and rotary). The horizontal positioning is accurate to 2 $\mu$m and the vertical positioning is accurate to 25 $\mu$m.

## 3.9 Safety

Since ultrasound uses acoustic waves that are non-ionizing, there exists no radiation hazards that are usually associated with x-ray imaging. The bioeffects that can result from the use of ultrasound fall into two groups: heating and mechanical (Kremkau, 1993). Tissue heating arises because of absorption – the energy that is absorbed by the tissues is converted to heat. Heating increases as the intensity of the ultrasound wave increases. Heating also increases with increasing frequency of operation, because there is more absorption at higher frequencies. For safe operation, the American Institute of Ultrasound in Medicine (AIUM) recommends that the temperature rise be less than 1 degree Celsius. The mechanical effect of ultrasound is cavitation, the production and collapse of bubbles in a liquid medium. Transient collapse of bubbles can produce shock waves, localized temperature rises, and even light emissions and is considered a significant destructive effect. The occurrence of cavitation is more likely at higher acoustic intensities.

In order to determine a safe operating environment in ultrasound, the AIUM recommends limiting the intensity and time of exposure. There are several intensity measures that are commonly used in practice in order to account for the non-uniformity of intensity across the sound beam, and non-uniformity in time (in the case of pulsed ultrasound). For example the intensity could be averaged or its peak value can be considered. The most commonly used measure in pulsed ultrasound is the spatial peak-temporal average value (SPTA), obtained by taking the peak intensity across the sound beam (spatially), while averaging the intensity in time. The SPTA value is used to determine whether the system is safe for use on humans (and other mammals). The AIUM recommends that an SPTA value of less than 1 W/cm$^2$ is safe. If the exposure time is less than 50 seconds, higher intensities can be used.

In our current system, the SPTA values are within the limits recommended by AIUM. The SPTA value is less than 13 $mW/cm^2$. This value is based on a similar, but more focussed transducer (Morgan *et al.* , 1996). The more focussed the transducer, the higher the intensity. Since the transducer used in this work is less focussed than the one reported in Morgan (1996), the system can be considered safe for use on human subjects.

# 4 Signal Processing and System Verification

## 4.1 Processing of raw signals

Converting the RF [1] echoes from the tissue into an image requires several steps. First, the received signal must be windowed to retain only the useful portion. Second, signal conditioning is needed to remove noise from the receiver electronics. Previous efforts in ultrasound tissue characterization experiments have shown that signal averaging greatly improves signal-to-noise ratio (SNR) and is almost a necessary step to improve the quality of the images. Next, a systematic way to determine the starting point of the signal is needed, as the exact distance between the transducer and tissue is not known *a priori*. Then, the reflected echoes which are at RF frequencies must be demodulated to baseband so that the envelope of the echoes can be obtained. Tissue contrast information is contained in the envelope of the reflected signal. Next, the signals should be modified to a dynamic range that is suitable for visualization. Then, the signals should be compensated for attenuation by applying higher weights to signals that came from deeper tissues, a process referred to as time-gain compensation. Finally, the scans from different lateral locations of the transducer should be combined to produce a 2D image. All the above steps are discussed in this chapter.

### 4.1.1 Windowing

A typical reflected echo is shown in Figure 4-1. The transducer was fixed at a particular location and was excited at a pulse repetition frequency (PRF) of 10 kHz. The object being imaged was the fingertip skin of a human subject. At a PRF of 10 kHz, the total

[1] Even though we deal with acoustic waves, the frequencies of interest correspond to that used in radio transmission using electromagnetic waves. Hence the echoes are referred to as radio frequency (RF) echoes.

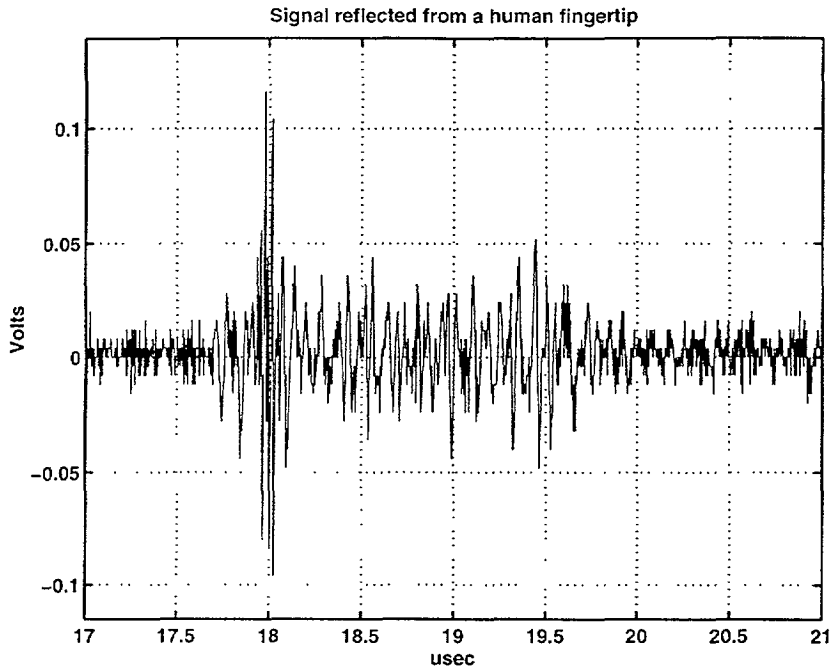


Figure 4-1: A typical (windowed) reflected echo from human fingertip skin. The x-axis is the time after transducer excitation. Useful signal starts to arrive about 17.5 to 18 $\mu$s after the transducer is excited and lasts for less than 4 $\mu$s. The first echo from the tissue is located to the left of the prominent peak, but is not clearly detectable because the noise is high. See also Figure 4-4 to see the effects of signal averaging on the SNR.

duration of each echo is 100 $\mu$s. However, because of attenuation, the useful signal from the tissue occurs for a much shorter period of time. For example, if the useful depth of imaging is 2 mm (which is determined by attenuation), the reflected echoes occur for only $2 \times 2\frac{\text{mm}}{1.5\ \text{mm}/\mu s} = 2.67\mu$s. The above calculation uses the fact that the speed of sound in most soft tissues is 1.5 mm/ $\mu$s, and the factor of 2 occurs because round trip times are computed. This is small compared to the pulse repetition period of 100 $\mu$s. Moreover since the tissue is placed at the focus of the transducer, it takes some amount of time to receive the first echo from the tissue. In Figure 4-1, the first echo from the tissue lies somewhere to the left of the prominent peak in the signal and occurs after a round trip delay between 17.5 and 18 $\mu$s. Recording only the useful signal is important because it reduces memory requirements especially when several acquisitions are to be stored. This is done during the acquisition stage by selecting a window that starts at 17 $\mu$s and has a total period of 4 $\mu$s.

### 4.1.2 Signal conditioning

The next step is to improve SNR. The RF signal reflected from the tissues contains noise from the receiver electronics. The receiver electronics has amplifiers, attenuators, low pass and high pass filters, all of which add noise to the reflected signal. For example, looking at Figure 4-1, it is not clear when exactly the first echo from the tissue occurs, because the low amplitude signals cannot be distinguished from noise. Previous studies have shown that signal averaging (averaging separate acquisitions) is important in tissue characterization studies (Cohn *et al.* , 1997a; Bridal and Berger, 1996). In order for signal averaging to improve SNR, the different acquisitions must be independent and each acquisition should have finite variance. In order to test if the different acquisitions are independent, 1000 acquisitions of noise were recorded. All the acquisitions were made when the transducer was immersed in water without any target to reflect the waves. The acquisition thus contains only noise from the electronics and minute reflections from water. Each acquisition was 100 points long. A particular sample (arbitrarily chosen) from each acquisition was chosen to test if these samples are independent from one another. Figure 4-2 shows the sequence of samples from the 1000 acquisitions, and its autocovariance. The autocovariance is seen to be mostly an impulse at the origin. Thus the sequence of samples from the different acquisitions can generally be considered independent and it is expected that averaging will help.

In order to calculate how much improvement in SNR can be obtained through averaging, the standard deviations of the noise after averaging N acquisitions, where N goes from 1 to 1000, were obtained. Figure 4-3 shows the plot of standard deviation as a function of the number of acquisitions used in averaging. If the acquisitions are independent, due to averaging the standard deviation of the noise will decrease by a factor of $1/\sqrt{N}$, and the slope of the log–log plot will be -0.5. It can be seen that initially the slope of the log–log plot is high (computed to be -0.501), but flattens as more acquisitions are used. This shows that taking more acquisitions leads to diminishing improvements in SNR. From a practical point of view, the number of signal acquisitions for averaging is limited mostly by the digitizer. More acquisitions require more memory for storage. The need to balance memory requirements with the need for averaging lead to a compromise in which 100 acquisitions each containing 1000 samples were averaged. A thousand points at 250

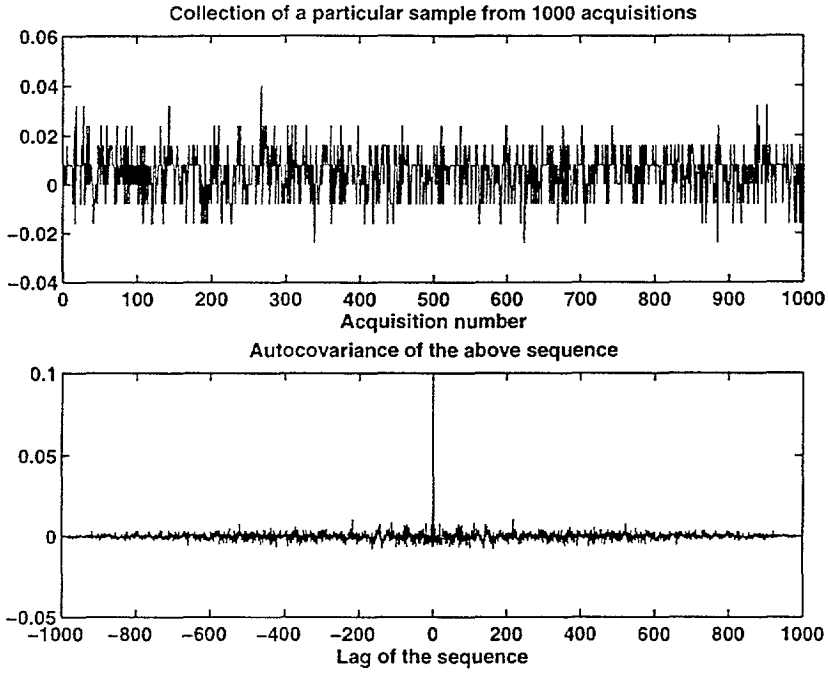


**Figure 4-2:** Test of independency of different acquisitions used in averaging. One thousand acquisitions of noise, each containing 100 samples were recorded. The sequence on the top panel was created by choosing a particular sample from each acquisition. The bottom panel shows the autocovariance of the sequence which is found to be mostly an impulse at the origin.

Million Samples/sec (MS/s) corresponds to a duration of 4 $\mu$s, which in turn corresponds to collecting reflected echoes from tissues as deep as 3.0 mm.

Figure 4-4 shows the effect of signal averaging. It can be seen that the noise level decreases due to averaging. Without averaging, it is not possible to see when the first echo from the tissue occurs. With averaging it becomes much easier to detect the location of the first echo.

Another advantage of signal averaging is the improvement in the number of bits per sample which leads to more quantization levels. Since quantization also introduces noise, the higher the number of bits for quantization, the lower the quantization noise. The quantization SNR improves by 6 dB per additional bit.

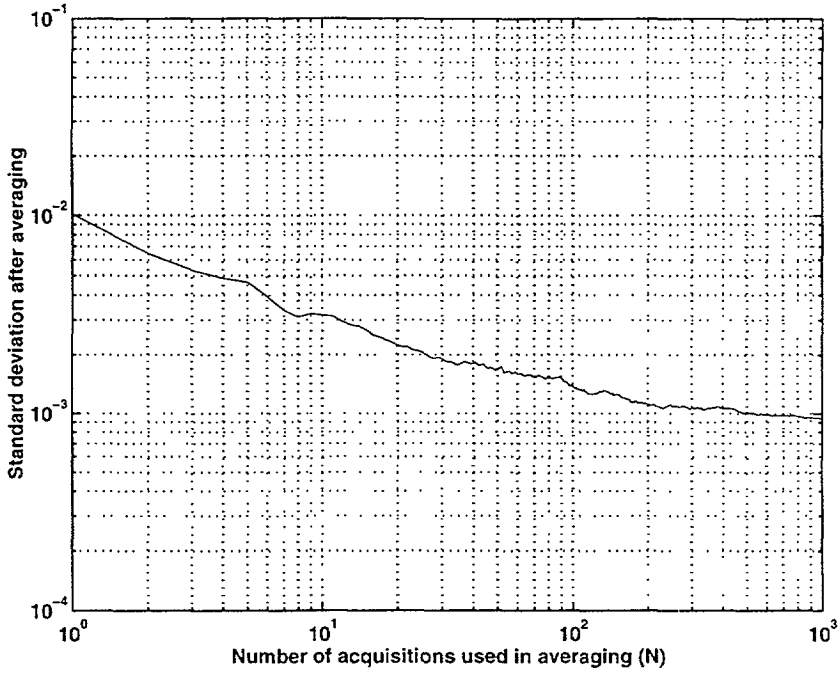


**Figure 4-3:** Standard deviation of noise decreases due to averaging. The decreasing slope with increasing number of acquisitions implies that improvements in SNR would decrease with increasing N.

### 4.1.3 Determination of starting point of the reflected RF signal

Determining the starting point of the useful signal simply requires a way to distinguish signal from noise. For example, in Figure 4-4 (b), up to about 17.70 $\mu$s the waveform only contains noise. In order to determine the starting point of the signal, the maximum absolute noise level in the waveform is first computed. This can be done by looking at the first few samples that are collected before the first echo from the tissue arrives. Then the time at which this noise level is exceeded is determined. The waveform that is collected after this time is then considered as the useful signal reflected from the tissues. For this technique to work, it is essential to collect some noise before the arrival of the first echo. This can be easily be ensured during the experiment by choosing an appropriate delay or by adjusting the distance between the transducer and tissue being imaged. It is also essential to have a reasonably large number of samples to estimate the noise level. In the actual experiments at least 100 samples (corresponding to 0.4 $\mu$s) were used to compute the noise level. Based on this method, the time of arrival of the first echo from the tissue in Figure 4-4 (b) was found to be 17.712 $\mu$s.

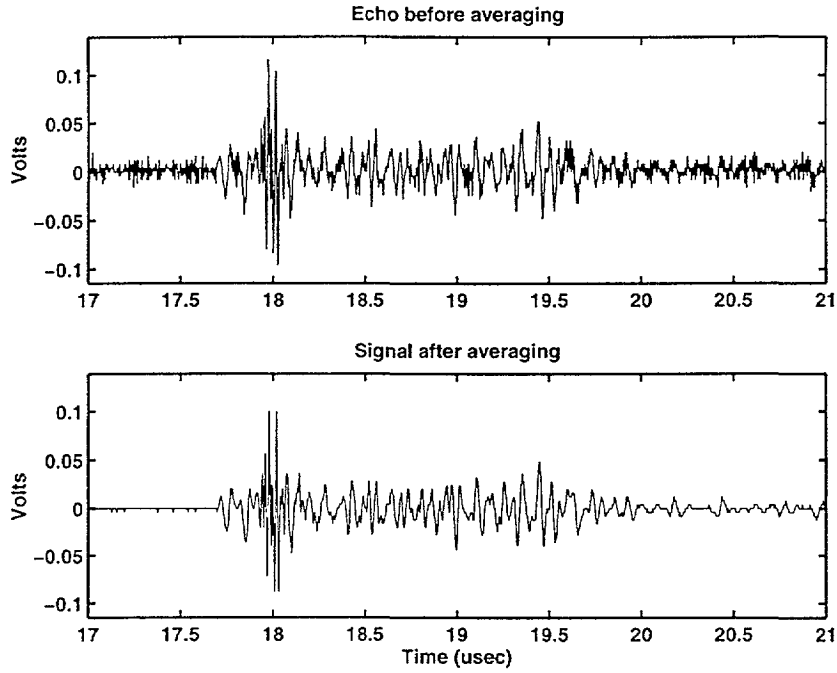


**Figure 4-4:** Signal averaging reduces noise level. The top figure is the signal before averaging. The bottom figure is the signal after averaging 100 independent acquisitions. The noise level decreases due to signal averaging. After averaging, it becomes easier to detect when the first echo from the tissue occurs (at 17.70 $\mu$s).

### 4.1.4 Extraction of tissue information from the reflected echoes

*Determination of the frequency characteristics of the transducer according to ASTM (The American Society for Testing and Materials) standards:*

Ultrasound signals are similar to AM radio signals which contain an RF carrier signal modulated by low frequency baseband signals. The center frequency of the transducer in ultrasound is analogous to the carrier frequency of the AM radio signal. The tissue contrast information is contained within a bandwidth around the center frequency. Thus extraction of tissue information is the extraction of the envelope of the reflected echoes by demodulating the RF echoes to baseband frequencies. In order to do this, the frequency characteristics (center frequency and bandwidth) of the transducer must be known. For this, the procedure described in the ASTM standards (American Society for Testing and Materials, 1992) was followed. The transducer was focussed at a glass plate whose thickness was much greater than the wavelength of the wave used. The reflected echo was digitized at 500 MS/s and the frequency spectrum was computed using the FFT function

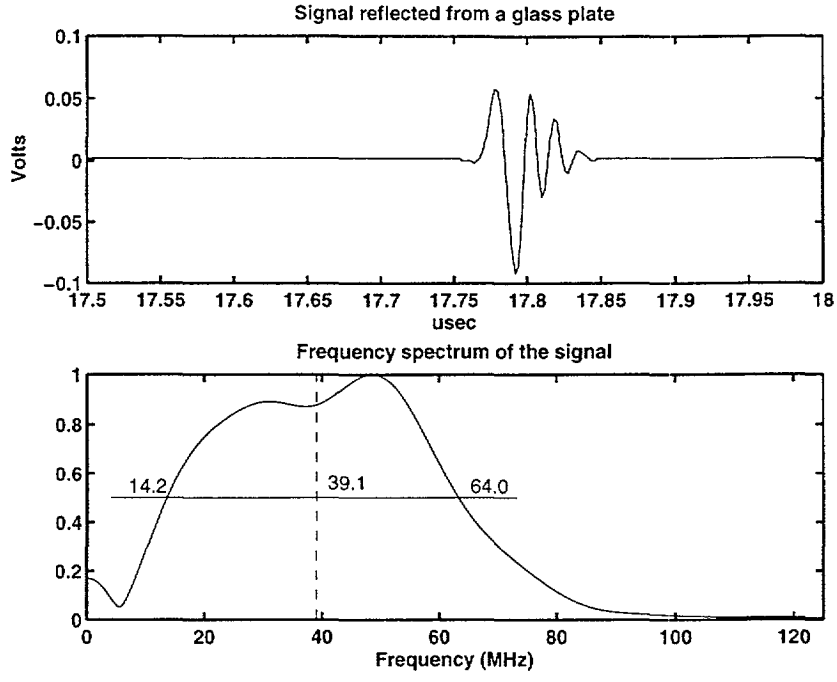


**Figure 4-5:** The top figure shows the signal reflected from a glass plate. The bottom figure shows the spectrum of the signal. The spectrum is based on the useful reflected signal at the center and does include the flat portions on either side of the signal. The center frequency is found to be 39.1 MHz and the -6 dB bandwidth is found to be 49.8 MHz.

in Matlab. Figure 4-5 shows the reflected echo and the corresponding frequency spectrum. The upper and lower bandwidth limits are computed as the frequencies at which the magnitude is 6 dB below the peak magnitude of the spectrum (i.e. at half of the peak magnitude). In Figure 4-5, the upper and lower bandwidth limits are found to be 14.2 and 64.0 MHz.. The center frequency is defined as the mean of the upper and lower bandwidth limits, even though it may be different from the peak frequency. The center frequency was found to be 39.1 MHz and the peak frequency was found to be 48.3 MHz.

*Demodulation of the RF echoes to baseband frequencies:*

Demodulation is done using digital filters after the reflected echoes are digitized. Demodulation is essentially applying a bandpass filter only to the positive frequencies of the RF signal and then taking the magnitude of the filtered signal. In order to do the bandpass filtering, a 64 point Finite Impulse Response (FIR) filter was chosen. An FIR filter was chosen because of its linear phase characteristics. The filter was designed using

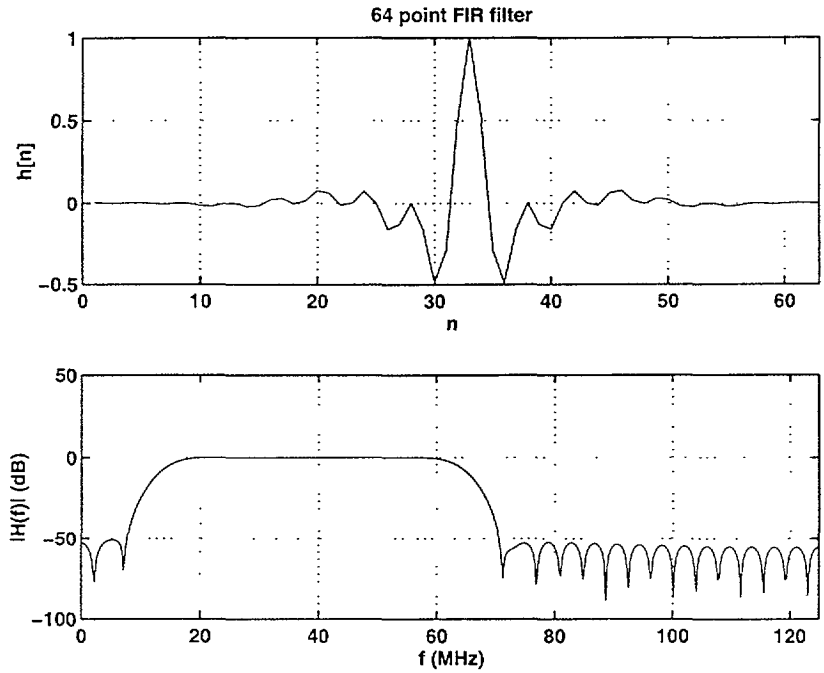


**Figure 4-6:** A 64 point FIR bandpass filter was used to demodulate the RF signals to baseband frequencies. The top figure shows the filter in the time domain and the bottom figure shows its frequency response.

the windowing method, using a Hamming window. Figure 4-6 shows the filter and its frequency response. The filtered signal is a complex baseband signal whose magnitude is the envelope signal containing tissue information.

### 4.1.5 Time-Gain Compensation

Since all tissues exhibit attenuation, the magnitude of the signals reflected from deeper tissues will be smaller than those reflected from tissues close to the surface. In order to compensate for this, the reflected signals are scaled by a weighting function that applies larger weights to signals coming after larger delays (i.e. from deeper tissues). The attenuation in dB is approximately linear with depth. Hence the simplest choice for the weighting function is a linear ramp function (when the gain is expressed in dB scale), as shown in Figure 4-7 (a). This function is useful only if there are no physical boundaries in the tissue being imaged. However physical boundaries such as the one between water and the topmost tissue always exist. The echoes from these boundaries will always have high reflection coefficients resulting in too high a contrast in those regions. In order to

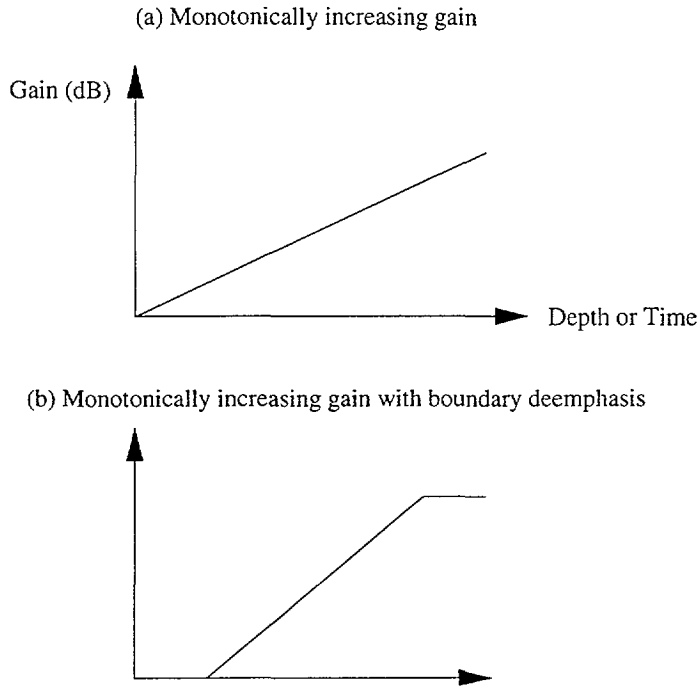


**Figure 4-7:** Two examples of time-gain compensation are shown. In (a), a linear (ramp) gain function is shown. In (b), a ramp function that deemphasizes physical boundaries is shown. The figure assumes that there are only two boundaries, one at the beginning and the other at the end.

deemphasize these boundaries, the gain function is chosen to have low values at these regions, an example of which is shown in Figure 4-7 (b). Likewise, in order to emphasize a certain feature in the image, the gain may be increased in certain regions. The numerical values for the gain function depend on the amount of attenuation in the tissue and usually comes from prior experience. In this work, a gain function similar to that in Figure 4-7 (b) is used. The amount of attenuation depends on the frequency of the wave used. The higher the frequency, the higher the rate of attenuation. The rate of the ramp function was chosen to be 0.5 dB/cm/MHz, which leads to 37.5 dB/cm at a frequency of 75 MHz. In commercial diagnostic ultrasound machines, compensation is usually done with analog circuits. In this work, compensation is done in Matlab after digitizing the signals.

### 4.1.6 Image generation

In order to make images visually suitable for humans, the signals are modified to a dynamic range that is suitable for viewing. In this work, the pixel values in the image are rescaled

so that they are distributed more uniformly — thus improving tissue contrast as perceived by our visual system. This procedure is described in Chapter 5. In order to create an image, the A-scans from different locations of the transducer are processed and combined together. Since the pixel density (# of pixels per cm) in the depth direction is not the same as that in the lateral direction, the image is resampled so as to have same the pixel density in both directions. The images are plotted using functions from the Image Processing toolbox in Matlab.

## 4.2 Lateral Resolution

This section describes the experiments that were performed to determine the lateral resolution of the system. In order to determine the lateral resolution, objects with known dimensions along the lateral direction are needed. A simple and accurate way to "create" these objects is to use a caliper. The gap between the two arms of the caliper can be adjusted to any value within an accuracy of 10 $\mu$m. The gap can then be imaged and the image can be compared with the actual profile of the gap. The width of the smallest gap for which the measured width does not vary appreciably from the actual width can then be taken to be the lateral resolution. In this study nine such "gaps" are used. The dimensions of these gaps (in microns) are 1500, 1000, 500, 240, 200, 160, 120, 80 and 40. The first three gaps are considered large gaps as they are expected to be much larger than the lateral resolution of the system and the other gaps are considered small. This distinction is somewhat arbitrary.

The reflected echoes from the gaps were obtained. The profile of the gap was constructed by plotting the magnitude of the echo reflected as a function of distance along the gap [2]. Figure 4-8 shows a comparison between the experimentally obtained profiles and the actual gaps for the case of the large gaps. It can be seen that at the edges, the signal drops in magnitude gradually, instead of falling down steeply. This is because of diffraction effects due to finite beam size. In order to determine the width of the gap as measured by the experiment, the following protocol was used: The experimentally measured width of the gap was taken to be the distance between the points at which the signal amplitude

[2]Since the caliper is made of metal and is homogeneous, the signal reflected is for all practical purposes a single echo. The amplitude of this echo can be used to obtain the profile.

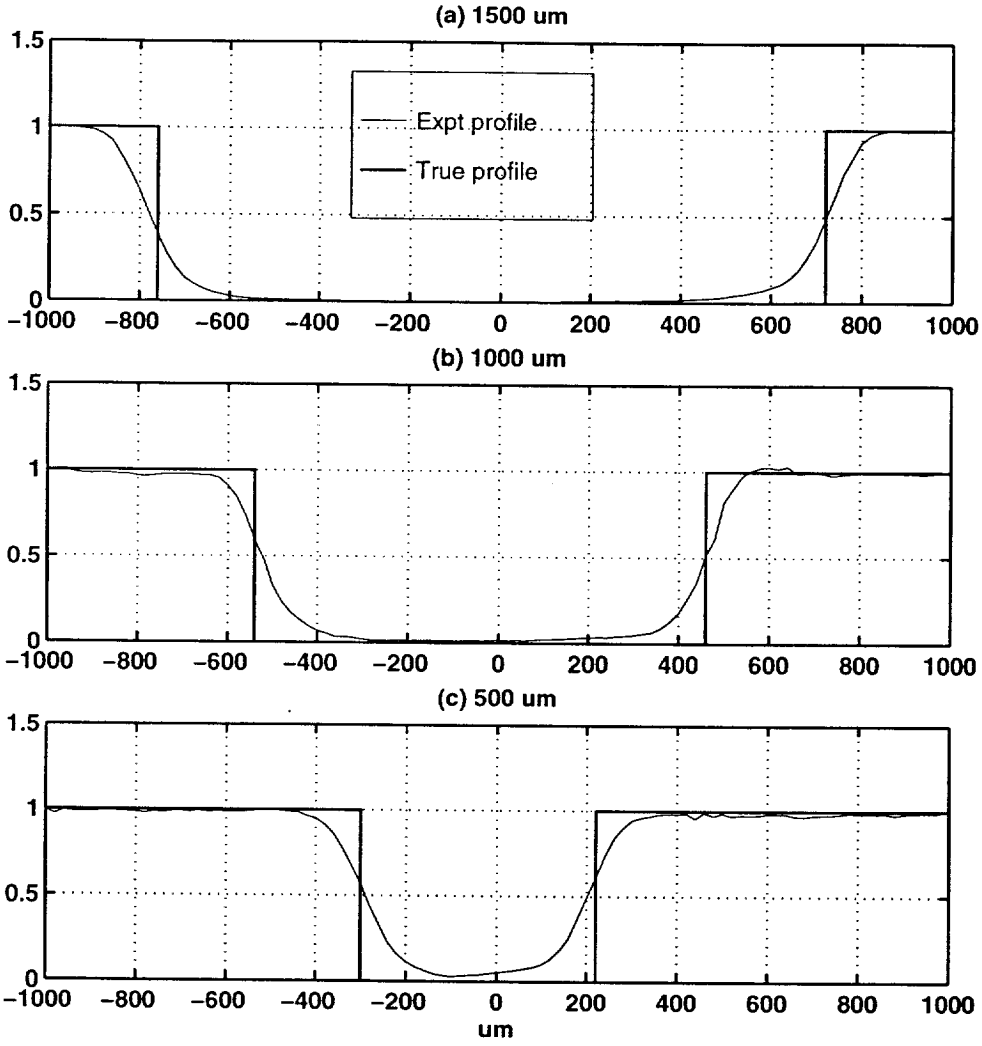


**Figure 4-8:** Comparison of experimentally obtained profiles and actual profiles for the case of large gaps. The values on top of each panel are the actual widths of the gaps. The experimental profiles are obtained by plotting the amplitude of the signal as a function of the location of the transducer. The experimentally obtained widths of the gaps (distance between the points at which the signal amplitude drops by one half), is found to be approximately the same as the actual widths.

falls by one half. Using this protocol, it can be seen that for all the three large gaps, the experimentally obtained widths are almost the same as the actual widths.

Figure 4-9 shows the comparison between the experimentally obtained profiles and actual profiles for the case of small gaps. It can be seen that the experimentally obtained widths match the actual widths for widths less than or equal to 160 $\mu$m. When the widths

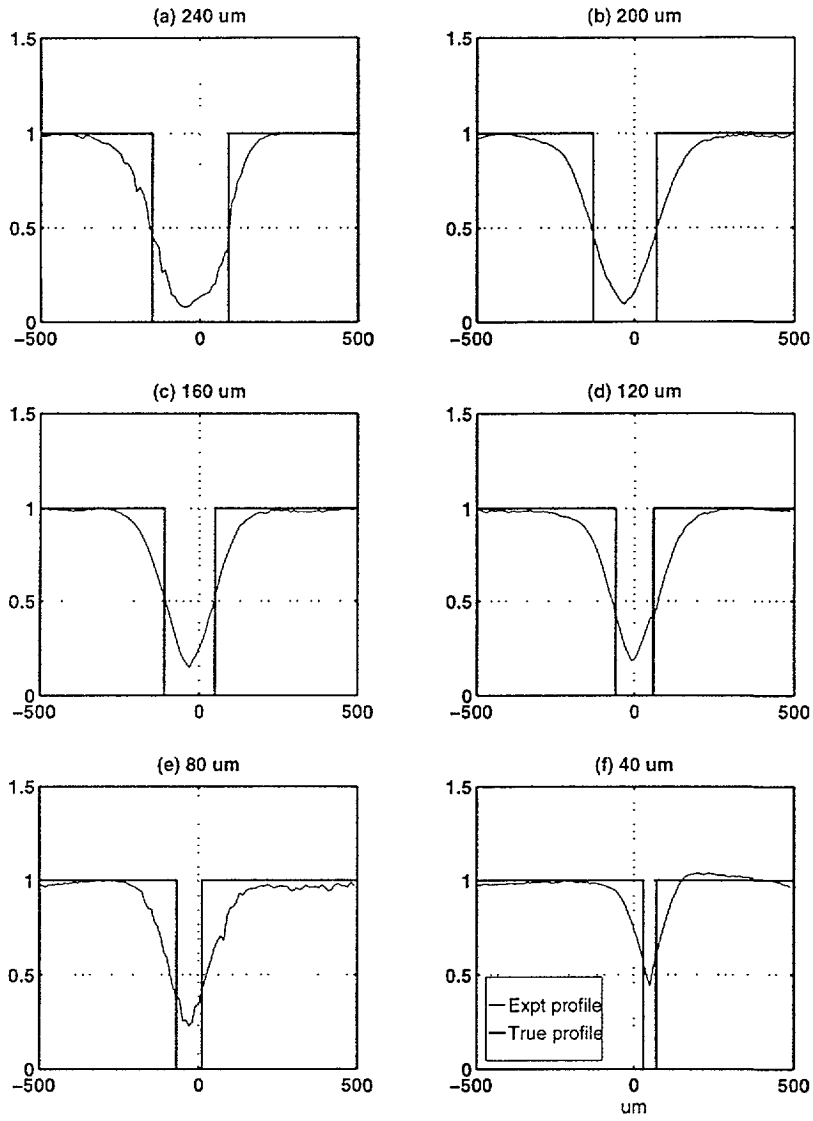


**Figure 4-9:** Comparison of experimentally obtained profiles and actual profiles for the case of small gaps. The values on top of each panel are the actual widths of the gaps.

are 120 and 80 $\mu$m, the experiment overestimates the widths. When the width is 40 $\mu$m, the experiment underestimates the width.

In order to determine when the system fails to accurately image the gaps, the absolute percentage error in the calculated widths were obtained for all the gaps. The width below which the percent error becomes greater than 10% is taken to be the smallest width that can be reliably imaged. Figure 4-10 shows the results. The percent error is small for high widths

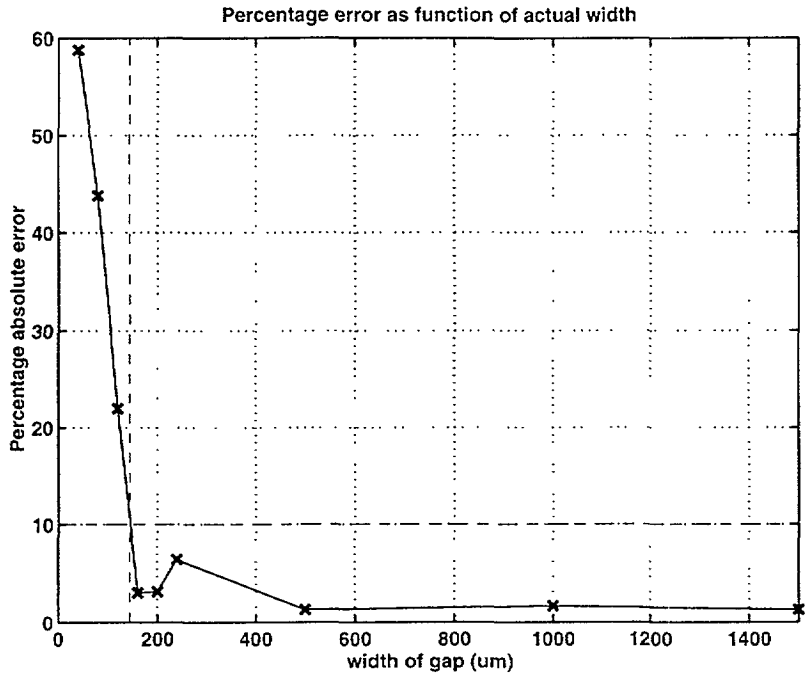


**Figure 4-10:** Percent (absolute) error in measuring gap widths. The error is greater than 10% when the width of the gap is less than 144 $\mu$m (shown by the vertical dotted line).

but quickly increases after about 160 $\mu$m. For widths less than about 144 $\mu$m, the percent error is greater than 10% and hence the lateral resolution of the system is taken to be 144 $\mu$m.

In order to ensure that the calculation of width is reliable, the experiment was tested for repeatability. The gap was fixed at 200 $\mu$m and the imaging was repeated ten times. The mean of ten trials was found to be 206.2 $\mu$m and the standard deviation was found to be 15.13 $\mu$m (7.3%). Two reasons could be cited for this variability. First, the beam size itself can have a statistical variability and need not be a constant. Second, there could be errors in scanning - the direction of scan may not be exactly perpendicular to the gap. The measured gap width could be greater than the actual gap width by a factor of $\cos(\theta)$, where $\theta$ is equal to 90° if direction is exactly perpendicular to that of the gap. Since the variability is a small percentage of the actual gap width, the experiment is taken to be quite reliable.

Another way to obtain the lateral resolution of the system is to compute the lateral (impulse) response function, that is, the function that describes how much the signal reflected from a point source is smeared. When the gaps are imaged, the experimentally obtained

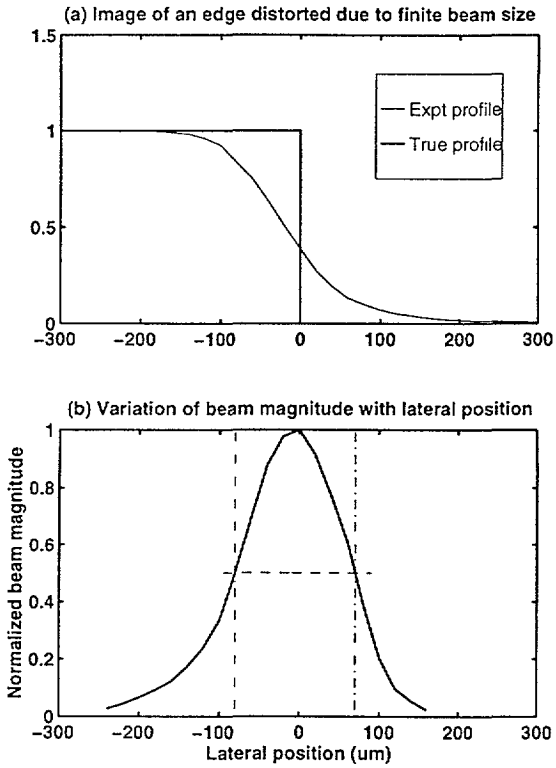


**Figure 4-11:** The top figure shows the smearing effect of the lateral response function. The bottom figure shows the lateral response function obtained by deconvolving the actual profile out of the experimentally obtained profile. The lateral resolution as measured by the full-width-at-half-maximum is found to be 149 $\mu$m.

profile is simply the convolution of the lateral response function and the actual profile. Hence simply deconvolving the actual profile out of the experimentally obtained profile gives the lateral response function. Figure 4-11 shows the lateral response function. The lateral resolution can be obtained from this as the full-width-at-half-maximum and its value is found to be 149 $\mu$m. This value is close to that obtained through the previous method which was based on errors in measuring widths.

## 4.3 Axial Resolution

The axial resolution of the device is the size of the smallest feature that can be resolved in the depth direction. In order to determine the axial resolution, shim plates with varying thicknesses were imaged, so that the thinnest plate for which echoes from the top and bottom surfaces can be separately distinguished can be determined. The plates were all

made of stainless steel and had the following thicknesses (in inches): 0.031, 0.015, 0.007, 0.004, 0.002 and 0.0015 [3]. The echo reflected from a 0.015 inch plate, after demodulation, is shown in Figure 4-12. The composite echo from the plate contains several echoes due to repeated reflections at the top and bottom plates. Since the speed of sound in stainless steel is known, thickness of the plate can be determined if the individual peaks can be clearly distinguished. It can be seen that for the case of 0.015 inch plate, this is indeed the case, as peaks A, B, ... can be separately distinguished.

Figure 4-12 also shows that subsequent peaks are decreased in magnitude (because of exponential attenuation). Magnitude of echo B is only about 15% that of echo A. If echo B occurs closer to echo A, which happens for thinner plates, then it will blur into echo A and will not be seen separately, simply because it had much less magnitude than that of A. If we had used tissues in this experiment, the attenuation would have been much less and echo B would be better distinguished from echo A, because it would have had a higher magnitude. Thus, for the case of steel plates, it is not desirable to compare echoes A and B. Hence, in all further analyses, echoes C and D (or even higher ones) were used to see if successive echoes are separately distinguishable.

Figure 4-13 shows two successive echoes for all the six plates. In order to determine when the two echoes are separately distinguishable, a protocol similar to that used in the previous section is used. When the two echoes merge at 50% (or higher) of their maximum amplitude, they are taken to be no longer separately distinguishable. In Figure 4-13 this happens for thicknesses below 0.004 inch (0.102 mm). Hence the resolution of the device in steel is 102 $\mu$m. It can be argued that for lesser thicknesses, for example 0.002 inch, it is still possible to see the two echoes separately. But this is only because the echoes happen to be of same magnitude. In the case of tissue imaging, the reflectivities of two adjacent tissue will not necessarily be equal. If one of the echoes is 50% of the other, then the smaller echo may not be distinguishable. Hence it is better to use the 50% protocol to determine the smallest thickness that can be imaged, rather than relying on whether the peaks can be visually seen separately. Thus the smallest thickness of the steel shim plates that can be imaged, with echoes from the top and bottom surface separately distin-

[3] $0.001 \text{inch} = 25.4 \mu\text{m}$

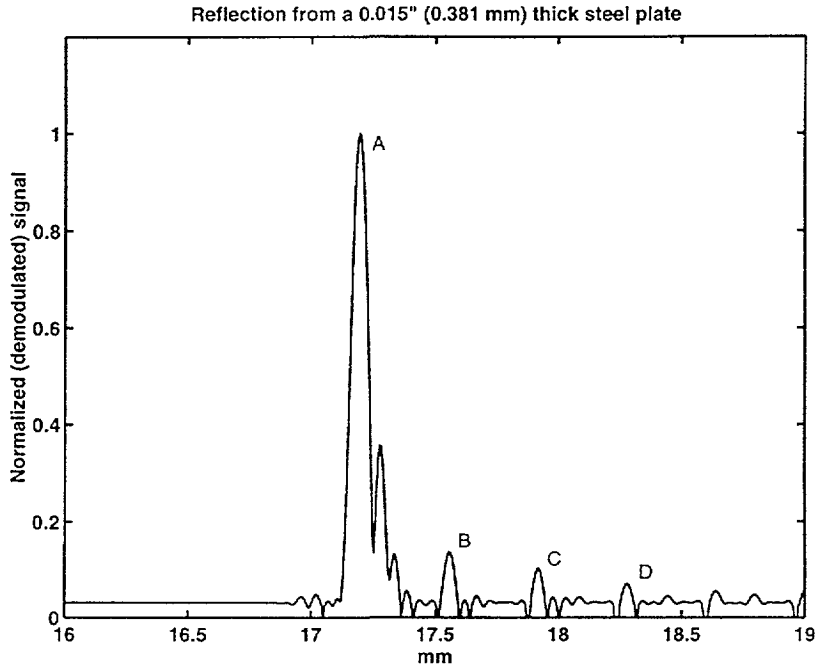


**Figure 4-12:** Echo from a 0.015 inch steel plate, after demodulation. Echo A is obtained from the top surface of the plate. Echo B is obtained from the bottom surface of the plate. Echoes C, D . . . are obtained due to multiple reflections at the top and bottom faces. Echo A itself contains more than one peak. Subsequent echoes (B, C . . . ) have lower magnitudes due to attenuation. The attenuation is frequency dependent and hence echoes B, C . . . are more low pass filtered.

guishable, is about 0.004 inch (0.102 mm), and the resolution of the device in steel is 102 $\mu$m.

In order to obtain the axial resolution in tissues, it is to be noted that the speed of sound in steel (6000 m/s) is four times that of the speed in soft tissues (1500 m/s). Hence the axial resolution of the device is four times better in tissues and is equal to about 0.025 mm (25 $\mu$m).

Another way to obtain the axial resolution is to compute the axial impulse response function, that is, the function that describes how much the echo from a hard, perfectly reflecting surface is smeared in the axial direction. If the system has infinitesimal axial resolution, the reflection from a hard surface will be an impulse function. However, as the ultrasound pulse itself is of finite width (see Equation 3.5) the echo from a hard surface is also spread out. Figure 4-14 shows the reflection from a glass plate after demodulation. The axial resolution can be computed as the full-width-at-half-maximum and is found to be 21 $\mu$m. This is close to that obtained by the previous method (25 $\mu$m).

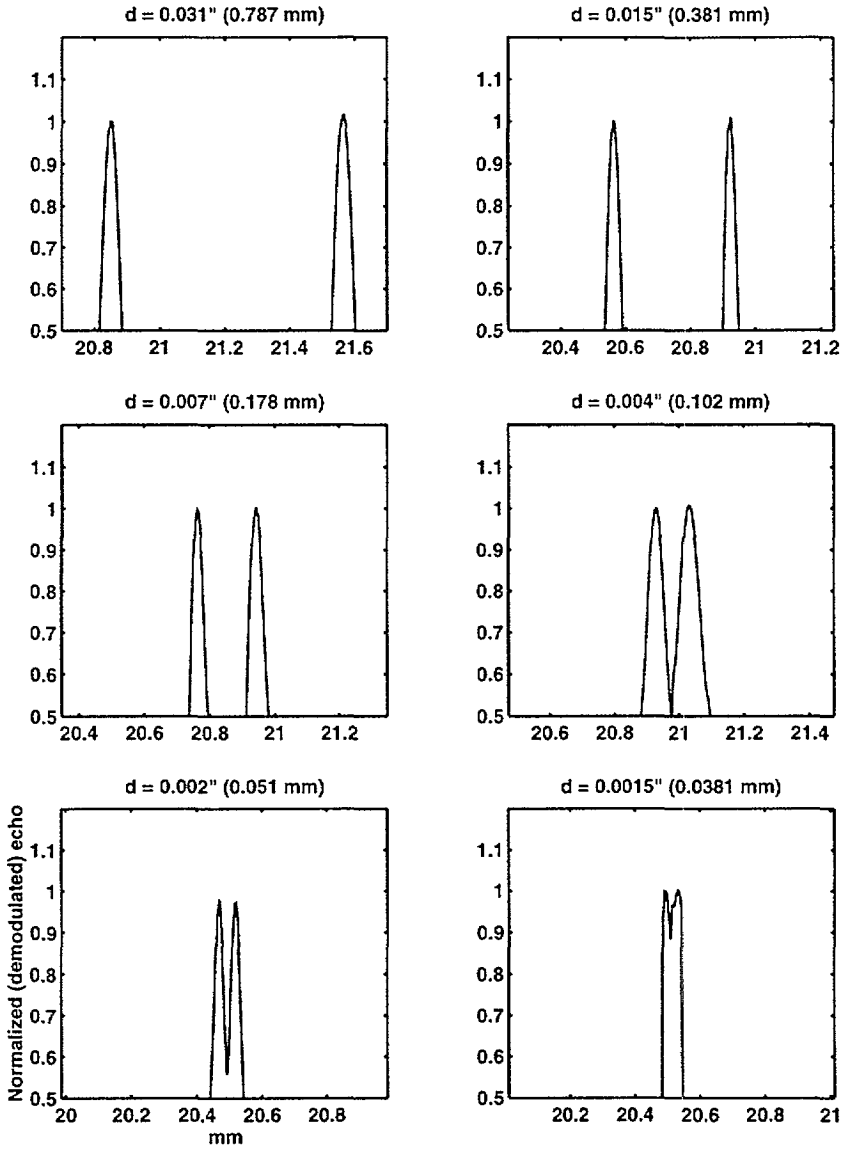


Figure 4-13: Axial resolution of the device. Two adjacent echoes from steel plates of different thicknesses are shown. The later echo was compensated for attenuation and hence appears to be of same magnitude. When the plate thickness is 0.004 inch (0.102 mm), the two echoes merge at half their maximum amplitude.

## 4.4 Imaging Tissue-Mimicking Phantoms

### 4.4.1 Need for imaging tissue phantoms

In the previous two sections the resolution of the device was evaluated based on reflections from metallic objects. These objects are homogeneous and result in reflections only at

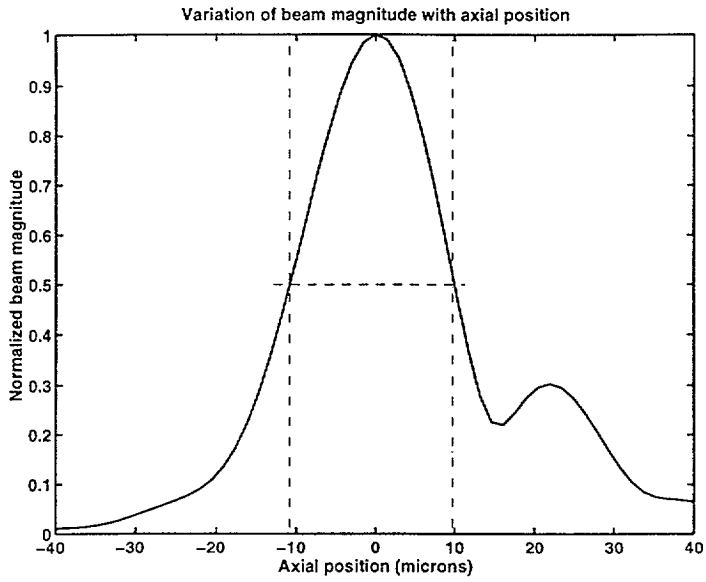


**Figure 4-14:** The reflection from a glass plate was demodulated to obtain the amplitude as a function of axial position (depth). This axial response function is spread out due to finite length of the ultrasound pulse used. The full-width-at-half-maximum is computed to be 21 $\mu$m.

the boundaries. However biological tissues are inhomogeneous by nature and result in reflections not only at tissue boundaries, but also in reflections from discrete points from within each tissue. Thus, while metallic objects can be used to determine the resolution capabilities of the system, they are not suited for determining the full functionality of the system. In order to verify the working of the system in a relevant context, several tissues with well known and distinct structures are needed. Due to practical problems it is difficult to obtain several such tissues, especially with features that are comparable to the resolution of the system, and features that are well documented in literature. Hence it was decided to use tissue-mimicking phantoms.

### 4.4.2 Preparation of the phantoms

Tissue phantoms for diagnostic ultrasound imaging are commercially available. But these phantoms are specifically prepared to be used at the frequencies used in diagnostic ultrasound machines ($<$ 15 MHz). For example, these phantoms are thick (about a cm or more) and have scatterers that are spaced by large distances (0.5 mm or higher). Hence these phantoms are not suitable for the current system that has lower depth of imaging and higher resolution. Moreover, since these phantoms are made for quality control purposes,

they are also expensive. Thus it is desirable to make phantoms *in situ*.

Graphite-gel phantoms in which the graphite particles serve as scatterers and the gel serves as a matrix are well suited for the purpose because of the ease of preparation. These phantoms were made according to the methods described in Cohn *et. al.* (1997b) and is summarized here for convenience. Ten percent by weight of gelatin is added to water and heated until the gelatin completely dissolves. Graphite particles with a mean size of 10 $\mu$m are added to the solution and stirred with a magnetic stirrer so as to ensure the graphite particles are uniformly distributed. The mixture is then quickly refrigerated so as to accelerate the hardening process of the gel, thus minimizing graphite settling at the bottom. The ratio of the gel to graphite (R) was varied to obtain phantoms with different graphite concentrations. The ratios were chosen to be 1:1, 4:1, 16:1, 64:1, 256:1, and inf:1 (i.e., no graphite was added).

### 4.4.3 Images of tissue-mimicking phantoms

Before a discussion of the phantom images is presented, it is useful to have a theoretical understanding of what to expect in these images. With decreasing concentrations of graphite, the images should generally show a decrease in the density of scatterers. The size of the particles is small compared to the wavelength of the wave and hence the type of scattering that occurs from the graphite particles is Rayleigh scattering. It can be shown that the power spectrum of the reflected echoes is approximately proportional to the density of the scatterers (Greenleaf and Sehgal, 1992). Thus the brightness of the image will be proportional to the density of the scatterers. Figure 4-15 shows the images obtained. It can be seen that with decreasing amount of graphite, the images show a decrease in the amount of scatterers. Also the brightness of scatterers decreases with decreasing graphite concentration. When no graphite is added (R = $\infty$) the image shows only a single boundary, except for some noise or dirt in the gel. Thus these images serve to verify the working of the system *qualitatively*.

It is to be noted that most of these phantoms except the ones that had very low graphite concentrations looked *homogeneously black*. Thus an optical technique (using visible light) would miss the presence of the scatterers when viewed directly. Ultrasound backscatter

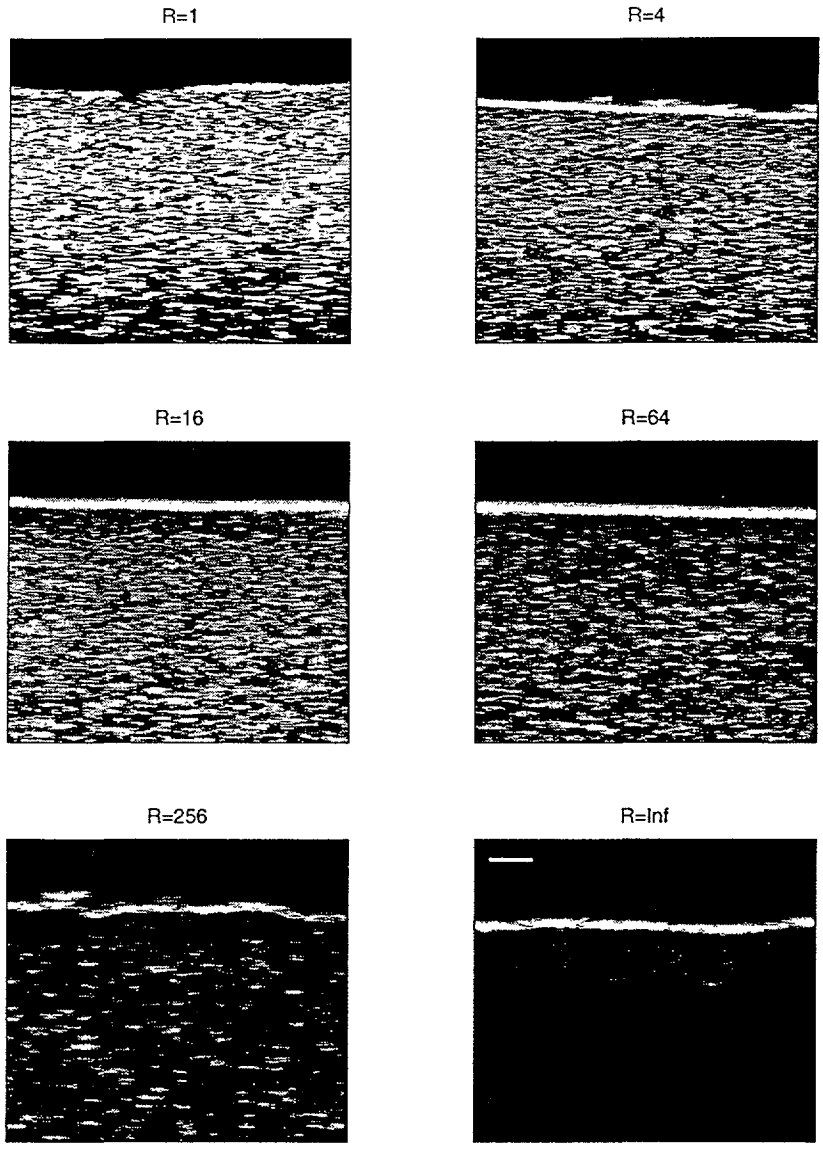


**Figure 4-15:** Images of graphite-gel phantoms. The value above each panel is the ratio of gel to graphite (by weight). The horizontal bar in the last panel (R = Inf) is 500 $\mu$m long.

microscopy uses changes in mechanical properties of the object to create an image and hence was able to show the presence of the graphite scatterers. This reiterates the fact that UBM complements other imaging modalities, and is better in terms of imaging features that have varying mechanical properties.

# 5 Fingertip Images

## 5.1 Experimental Protocol

Imaging of fingerpad skin was done on six subjects, four males and two females (denoted as M1, M2, M3, M4, F1 and F2). For all the subjects, the left index finger was used. Only the tip of each finger was imaged. The subject was comfortably seated and his/her left hand was placed in a water bath. In order to minimize artifacts due to movement of the finger, a custom-designed thermopolymer splint was made for each subject's finger. Figure 5-1 shows the experimental setup. The scope was set up to acquire and average 100 echoes, each containing 1000 points. The sampling rate used was 250 MS/s, which corresponds to an imaging depth of 3 mm. Prior to imaging, the transducer was adjusted until it was about 0.5 inch from the finger surface. Since the finger is curved, the distance between the transducer and the finger will not be constant when the transducer is stepped across laterally. Hence care was taken to ensure that the signals lie within a 4 $\mu$s window (see Section 4.1). During imaging the subject was asked to sit still. The transducer was stepped manually 100 times in increments of 40 $\mu$m each, for a total scan distance of 4 mm and at each location echoes from the finger were recorded. The total time for imaging was less than 4 minutes. The raw data from the experiment was transferred to a workstation for processing into images.

Images of finger skin on the dorsal side (back of the finger) were also obtained from three subjects (M1, M3 and F2). The right index finger of each subject was used.

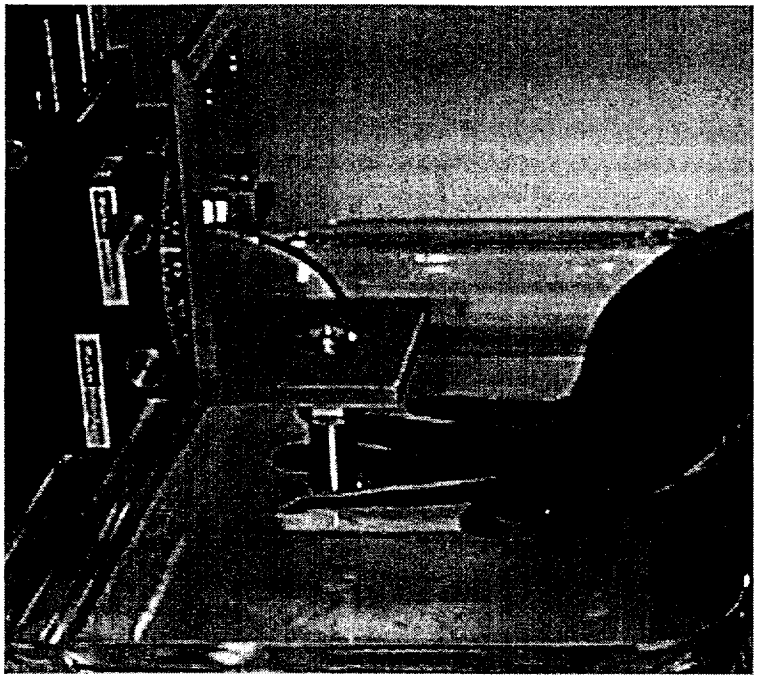

**Figure 5-1:** Experimental setup for fingertip imaging. The index finger was fitted with a custom-designed thermopolymer splint to minimize motion artifacts. The cylindrical object above the finger is the transducer. The transducer is immersed in water because the impedance of the transducer matches that of water and therefore reflections from the transducer-water boundary will not occur.

## 5.2 Image Processing

In UBM, the image contrast depends on the differences in mechanical properties of tissues as the wave goes from one tissue to another. Thus the images obtained using UBM may not be directly suited for our visual system. For this reason it is necessary to process the acoustic data before they are displayed as visual images. The most commonly used processing is gray level mapping. This consists of remapping a range of pixel intensities into another range of pixel intensities. The mapping could be either linear or non-linear. This procedure is explained using the image from subject F1. Figure 5-2 (a) shows the mapping employed in this example. All pixel intensities in the range 0 to 0.06 are mapped linearly to the range 0 to 1. Also all intensities greater than 0.06 are mapped to 1. A pixel with a value 0 is black and that with a value 1 is white. The mapping in Figure 5-2 was obtained by trial and error so that the image had good contrast. The mapping used for different subjects differed slightly from one another. Figure 5-2 (b) shows the histogram

of the pixels in the fingertip image before the mapping. It can be seen that most of the pixels have an intensity close to zero. Hence the image in Figure 5-2 (d) looks mostly dark. Figure 5-2 (c) shows the histogram of the pixels after the mapping. It can be seen that the mapping has expanded the pixel intensities to fill a bigger range. The image after mapping in Figure 5-2 (e) has better contrast in terms of tissue identification. The mapping was done using the **imadjust** function in Matlab's Image processing toolbox.

## 5.3 Broad Anatomical Correlations of Fingerpad Skin Images

Figure 5-3 shows the images of the fingerpad skin of six subjects. Since these images are preliminary, only broad anatomical correlations are possible at this time. The images from the six subjects are different from one another, but show some similarities. All the images show at least three layers running parallel to the skin's surface – there is a top layer which is bright, followed by an intermediate layer which is dark, followed by a deeper layer which is of intermediate brightness. This feature is clearest in images from subjects F2, M2 and M3. The thickness of these layers were measured by zooming the images and marking, using mouse buttons at locations where the intensities seemed to change visually. This process was done five times for each image and mean thicknesses were obtained for each subject. This process is subjective and small differences in thicknesses should be ignored. Table 5.1 shows the mean thicknesses for each subject. The first layer has a thickness of about 415 $\mu$m. Previous studies using histology and MRI techniques show that the thickness of the stratum corneum in the fingertip is about 400 $\mu$m (Voss and Srinivasan, 1998). Thus it is possible that the first layer seen in the images is the stratum corneum. The sum of the thicknesses of the first two layers is found to be 705 $\mu$m. From anatomical studies, the thickness of the epidermis in the fingertip is known to vary between 750 $\mu$m and 900 $\mu$m (Thomine, 1981). Thus it is possible that the first two layers seen in the images together constitute the epidermis. The thickness of the third layer, 463 $\mu$m, is less than the known thickness of the dermis. Hence the third layer is probably part of the dermis, possibly the reticular layer.

It can be seen that the images show a waviness at the top which probably corresponds to the finger ridges. These ridges are not very clear due to two reasons: First the lateral

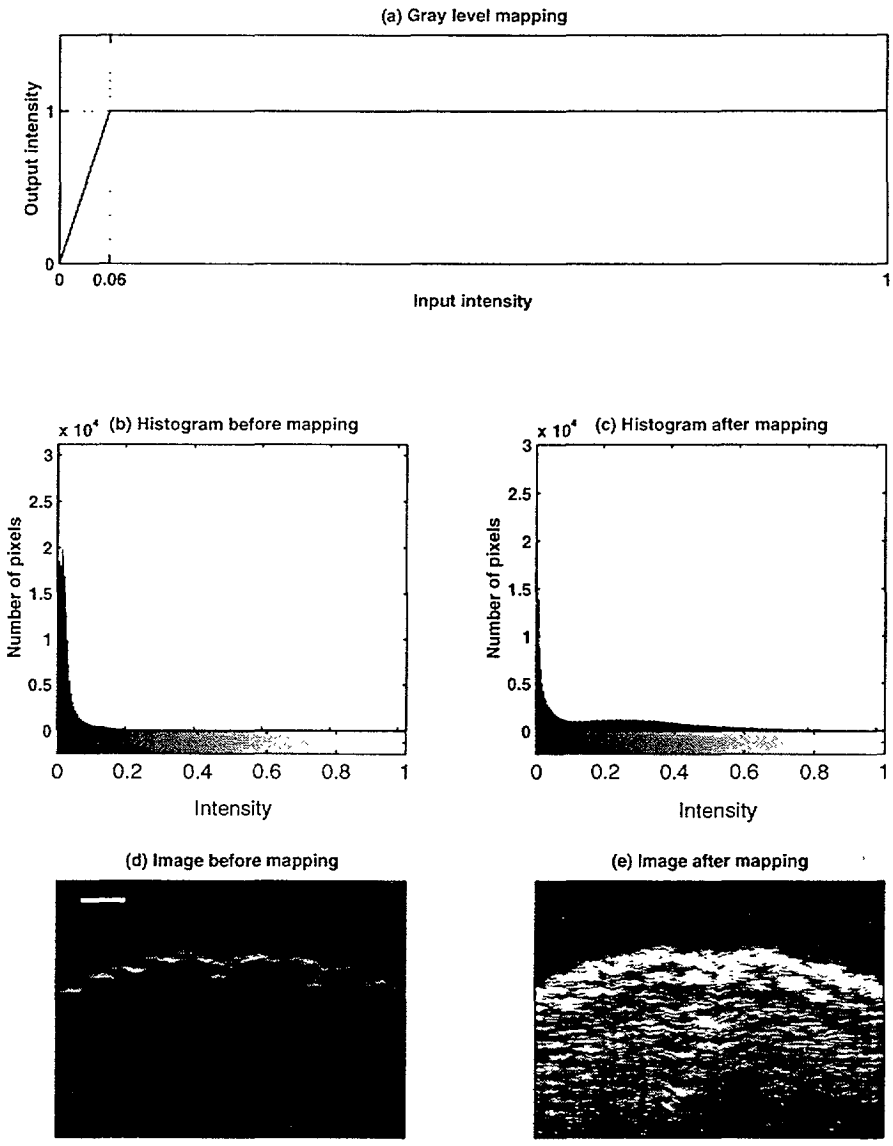


**Figure 5-2:** Gray-level mapping. The top panel shows that all pixels having intensities in the range 0 to 0.06 are linearly mapped to the range 0 to 1. All intensities greater than 0.06 are also mapped to 1. Panels (b) and (c) show the image histograms before and after the mapping. Panels (d) and (e) show images of fingertip of subject F1 before and after the mapping. The horizontal bar in panel (d) is 500 $\mu$m long.

| Subject | $t_1$( $\mu$m) | $t_2$( $\mu$m) | $t_3$( $\mu$m) | $t_1 + t_2$( $\mu$m) | $t_1 + t_2 + t_3$( $\mu$m) |
|---|---|---|---|---|---|
| F1 | 377 | 339 | 492 | 716 | 1208 |
| F2 | 438 | 298 | 498 | 736 | 1234 |
| M1 | 388 | 262 | 584 | 650 | 1234 |
| M2 | 436 | 295 | 356 | 731 | 1087 |
| M3 | 395 | 272 | 462 | 667 | 1129 |
| M4 | 458 | 274 | 385 | 732 | 1117 |
| Mean | 415 | 290 | 463 | 705 | 1168 |

**Table 5.1:** Comparison of thicknesses of the three layers seen in the fingerpad skin.

resolution of the system is not high enough and neighboring ridges get smeared into each other. Second, it was not possible to orient the scan exactly perpendicularly to the direction of the ridges. The internal ridges at the epidermal-dermal border are not seen at the present resolution and contrast.

It can be seen that it is possible to image at least one and a half mm from the surface. Beyond that depth, it is not clear whether the tissues there are poorly reflecting, or whether the attenuation is severe enough to prevent further penetration.

## 5.4 Images of Dorsal Skin

One way to check if the device is working properly is to image a tissue that has known differences compared to the fingerpad skin tissue. The dorsal skin on the back of the finger was chosen for this purpose. It is known from anatomy that the stratum corneum is thickest in the palms and soles, and thinner at other places, especially in the hairy skin. Figure 5-4 shows the images. It can be seen that the thickness of the first layer is much smaller than that of the fingerpad skin. Subjects F2 and M3 also show a thin second dark layer immediately below the first layer. Subject M1 does not show this dark layer very clearly. The average thickness of the first layer based on the three subjects was computed to be 235 $\mu$m and the average thickness of the second layer based on subjects F2 and M3 was computed to be 123 $\mu$m.

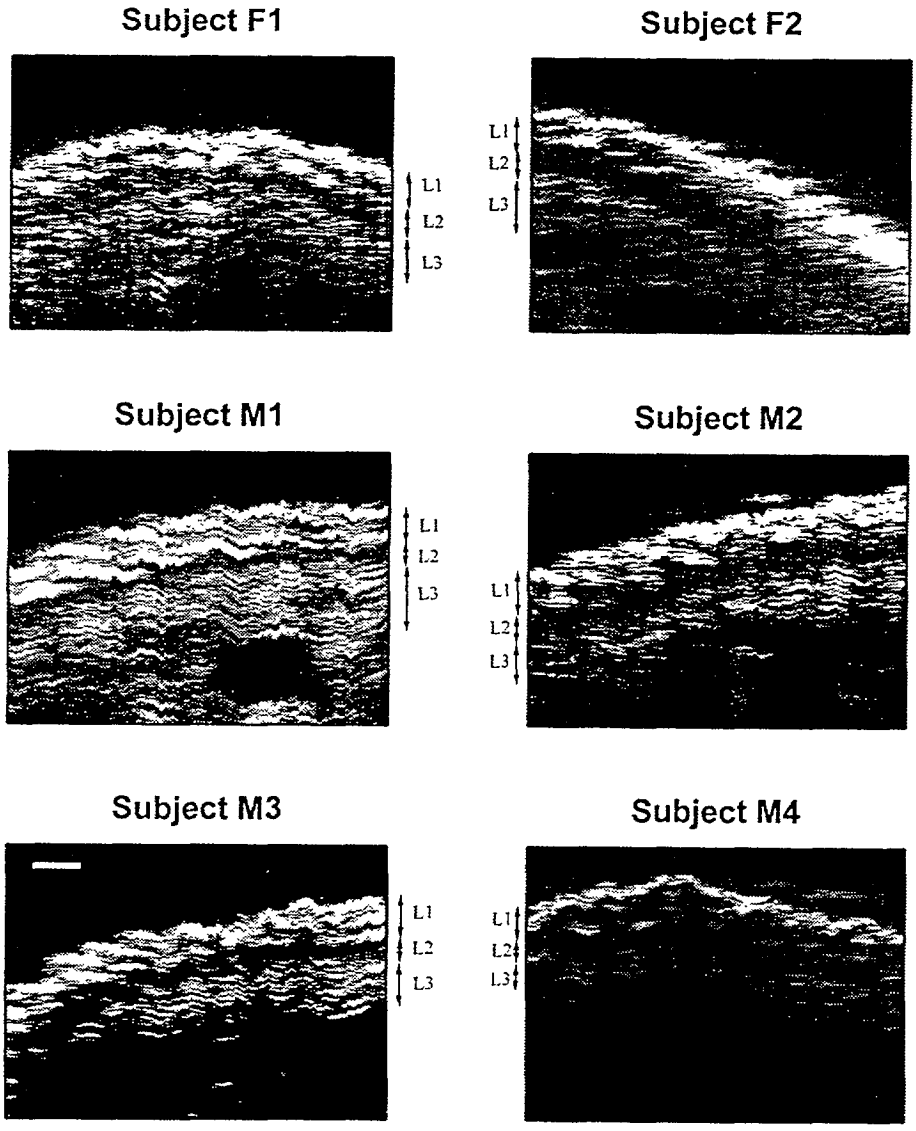


**Figure 5-3:** Images of fingerpad skin of six subjects. The left index finger was used for all the subjects. The horizontal bar in the image of subject M3 is 500 $\mu$m long. The resolution in the horizontal direction is 150 $\mu$m and the resolution in the vertical direction is 20 $\mu$m. The images from the six subjects are different from one another, but have a similarity in that at least three layers (denoted as L1, L2 and L3) running parallel to the surface can be seen in all the images. The top layer is bright, the second layer is dark, and the bottom layer is of intermediate brightness. The markings are not drawn to scale. The three layers are seen more clearly in the images from subjects F2, M2 and M3. In the case of subjects F1 and M1, there seems to be a second bright layer below the top bright layer, but this is more likely to be the interface between the first and second layers.

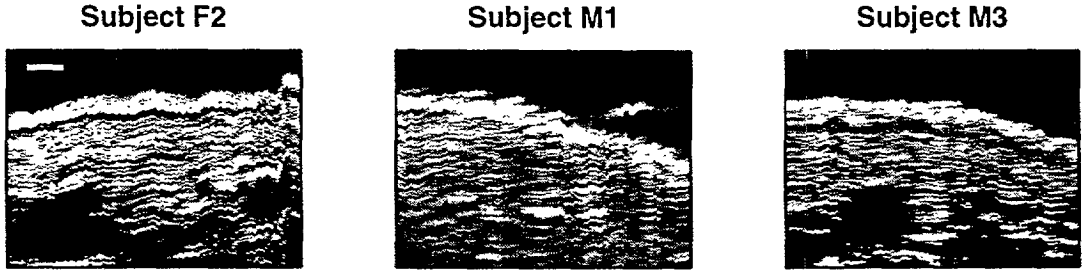


Figure 5-4: Images of dorsal skin on the back of the finger of three subjects. The horizontal bar in the image of subject F2 is 500 $\mu$m long. The dorsal skin looks different from fingerpad skin (see Figure 5-3) in that the thickness of the top layer is smaller than that of the fingerpad skin. The second dark layer is not seen clearly for subject M1. The separate strand originating from the surface seen in the image from subject M1 is probably a hair.

## 5.5 Problems in Fingertip Imaging

Several problems that are not encountered during imaging of inanimate objects occur during *in vivo* fingertip imaging. Obviously the body and hand posture should be comfortable to the subject. Also since the finger should be stationary, the setup should be ergonomic, so that the subject does not move because of discomfort. The size of the water bath, height of the table in which the experimental setup is placed, and the support for the forearm of the subject were all adjusted so as to make the setup comfortable for the subject. Still, since the imaging time was a few minutes, it is quite difficult to hold the finger stationary for that period of time. This is likely to have resulted in some loss of resolution in the fingertip images. It is expected that a motorized scanning system with a faster image acquisition rate will reduce this problem.

During the experiment it was noticed that tiny air bubbles sometimes settle on top of the finger, especially towards the end of the imaging session. Since air has different acoustic properties than water, reflections would occur at the boundaries of these bubbles. Hence the imaging had to be repeated to ensure that the images were taken when there were no air bubbles.

Because of poorer lateral resolution, some structures in the finger appeared elongated in the lateral direction. It is expected that a more focussed transducer will be able to

provide better lateral resolution and reduce this artifact.

It is to be pointed out that some of the usual problems encountered in diagnostic ultrasound imaging systems such as reverberation (Kremkau, 1993) do not seem to appear in the fingertip images. Reverberation is the production of multiple echoes from a finite sized, strongly reflective target, with each echo appearing later in time (see Figure 4-12). This leads to the appearance of multiple images of the same object, with the later images appearing dimmer due to attenuation. Such an artifact does not seem to occur in the fingertip images.

## 5.6 Problems in Interpreting the Fingertip Images

Interpreting the fingertip images is made difficult because of the following reasons:

- At present only anatomical information about the fingertip is known. Even that is based mostly on optical imaging techniques. However UBM relies on acoustic (mechanical) properties of the tissues and hence it is difficult to directly compare the "acoustic images" with existing anatomical information.
- Quantitative information of fingertip tissues, such as the height, and spacing between the finger ridges is not known.
- There are variations from one subject to another.
- Interpretation is further limited by poor lateral resolution.

Despite these problems, the UBM images are significant because they are, to date, one of the highest resolution images taken of the fingertip under *in vivo* conditions. Also, the dependence of contrast on mechanical properties implies that they provide an entirely different way of "looking" at tissues.

# 6
# Summary and Future Work

This thesis describes the development, verification and an application of the ultrasound backscatter microscope. The technique is suited for high resolution imaging of tissues that lie within a few mm from the surface. The system was built in the laboratory using a high frequency transducer, digitizer, pulser and scanning system. The axial resolution and lateral resolution were experimentally measured to be 20 and 150 $\mu$m respectively.

The technique was used to obtain fingertip images under *in vivo* conditions. The images of fingerpad skin from six subjects had similarities in the overall structure. At least three separate layers running parallel to the surface of the skin was seen. It is likely that the first layer corresponds to the stratum corneum of the epidermis and that the second layer corresponds to rest of the epidermis. The third layer is probably the reticular portion of the dermis. While these images are probably the highest resolution images of the fingertip under *in vivo* conditions to date, the resolution and contrast were still not enough to observe the internal ridges at the epidermal-dermal border. Images of finger skin on the dorsal (back) side were also obtained from three subjects. These images also showed a three layer structure, but the first two layers were thinner than that of the fingerpad skin. This agrees with known anatomical information.

The present work could be continued in several directions. The lateral resolution of the device could be improved by using more focussed transducers. This might lead to better images of the fingertip with clearer finger ridges on the surface, and possibly visualization of the internal ridges.

Currently manual scanning, which leads to an increased imaging time is used. Automating the scanning using computer-controlled motors would lead to less imaging time and

consequently less motion artifacts.

The use of advanced signal processing techniques such as synthetic aperture imaging could be investigated. Such techniques have led to superior lateral resolution in other fields like radar.

The usefulness of the device in other applications can be investigated. For example, the device might prove useful in imaging skin tumors, as the tumor usually lies close to the skin surface and has different mechanical properties from that of normal skin.

The device can be used to image tissue deformations in the fingertip. This can be done by taking a second image after indenting the finger with a known object. The movement of pixels could then be used to compute displacements, and consequently strains inside the finger. Such a study will be a direct extension of the current work and would aid in a deeper understanding of the mechanistic basis of tactile sense.

# References


American Society for Testing and Materials, , "A standard guide for evaluating characteristics of ultrasonic search units," *ASTM Standards*, vol. E1065-92, 1992.

Bolanowski, S. J., Gescheider, G. A., Verillo, R. T., and Checkosky, C. M., "Four channels mediate the mechanical aspects of touch," *J.Acoust.Soc.Am*, vol. 84, no. 5, pp. 1680–1694, 1988.

Brezinski, M. E., Tearney, G. J., Bouma, B. B., Izatt, J. A., Hee, M. R., Swanson, E. A., Southern, J. F., and Fujimoto, J. G., "Optical coherence tomography for optical biopsy, properties and demonstration of vascular pathology," *Circulation*, vol. 93, pp. 1206–1213, 1996.

Bridal, S. L. and Berger, G., "Local backscatter ultrasonic attenuation measurements in vitro (30 to 50 MHz) of the constituents of atherosclerotic plaques," *Ultrasonics Symposium*, pp. 1069–1072, 1996.

Briggs, A., *Acoustic Microscopy*. Clarendon Press, Oxford, UK, 1992.

Christensen, D. A., *Ultrasonic Bioinstrumentation*. John Wiley and Sons, New York, 1988.

Cohn, N. A., Emelianov, S. Y., Lubinski, M. A., and O'Donnell, M., "An elasticity microscope - Part 1: Methods," *IEEE Transactions on Ultrasonics, Ferroelectrics, and Frequency Control*, vol. 44, no. 6, pp. 1304–1319, 1997a.

Cohn, N. A., Emelianov, S. Y., and O'Donnell, M., "An elasticity microscope - Part 2: Experimental results," *IEEE Transactions on Ultrasonics, Ferroelectrics, and Frequency Control*, vol. 44, no. 6, pp. 1320–1331, 1997b.

Dandekar, K. and Srinivasan, M., "Role of mechanics in tactile sensing of shape," *RLE TR-604, MIT*, 1996.

Darian-Smith, I., "The sense of touch: Performance and peripheral neural processes," *Handbook of physiology - The nervous system -III*, pp. 739–788, 1984.

Devey, G. B. and Wells, P. N. T., "Ultrasound in medical diagnosis," *Scientific American*, vol. 238, no. 5, pp. 98–112, 1978.

Foster, F. S., Pavlin, C. J., Starkoski, B., and Harasiewicz, K., "Ultrasound backscatter microscopy of the eye *in vivo*," *Ultrasonics Symposium*, pp. 1481–1484, 1990.

Foster, S., "Medical and biological imaging with high frequency ultrasound," *IEEE Transactions on Ultrasonics, Ferroelectrics, and Frequency Control*, vol. 42, no. 4, pp. 485–485, 1995.

Foster, S., Pavlin, C. J., Lockwood, G. R., Ryan, L. K., Harasiewicz, K. A., Berube, L., and Rauth, M., "Principles and applications of ultrasound backscatter microscopy," *IEEE Transactions on Ultrasonics, Ferroelectrics, and Frequency Control*, vol. 40, no. 5, pp. 608–617, 1993.

Fung, Y. C., *Biomechanics*. Springer, New York, 1981.

Goodwin, A. W., John, K. T., and Marceglia, A. H., "Tactile discrimination of curvature by humans using only cutaneous information from the fingerpads," *Experimental brain research*, vol. 86, pp. 663–672, 1991.

Greenleaf, J. and Sehgal, C., *Biological System Evaluation with Ultrasound*. Springer-Verlag, New York, 1992.

Gulati, R. and Srinivasan, M., "Determination of mechanical properties of the human fingerpad , in vivo, using a tactile stimulator," *RLE TR-606, MIT*, 1996.

Hill, C. R., *Physical Principles of Medical Ultrasonics*. Ellis Horwood Limited, Chichester, UK, 1986.

Ho, C.-H. and Srinivasan, M., "Human haptic discrimination of thickness," *RLE TR-608, MIT*, 1996.

Huang, D., Swanson, E., C P Lin, J. S. S., Stinson, W. G., Hee, W. C. M. R., Flotte, T., Gregory, K., Puliafito, C. A., and Fujimoto, J. G., "Optical coherence tomography," *Science*, vol. 254, pp. 1178–1181, 1991.

Johansson, R. S., "Tactile sensibility in the human hand: Receptive field characteristics of mechanoreceptive units in the glabrous skin area," *J. Physiol*, vol. 281, pp. 101–123, 1978.

Johansson, R. S. and Vallbo, A. B., "Tactile sensibility in the human hand: Relative and absolute densities of four types of mechanoreceptive units in glabrous skin," *Journal of Physiology (London)*, vol. 286, pp. 283–300, 1979.

Johansson, R. S. and Vallbo, A. B., "Tactile sensory coding in the glabrous skin of the human hand," *Trends in Neuroscience*, vol. 6, pp. 27–32, January 1983.

Knibestol, M., "Stimulus-Response functions of rapidly adapting mechanoreceptors in the human glabrous skin area," *J. Physiol*, vol. 232, pp. 427–452, 1973.

Knibestol, M., "Stimulus-Response functions of slowly adapting mechanoreceptors in the human glabrous skin area," *J. Physiol*, vol. 245, pp. 63–80, 1975.

Knibestol, M. and Vallbo, A., "Single unit analysis of mechanoreceptor activity from the human glabrous skin," *Acta Physiol Scand*, vol. 80, pp. 178–195, 1970.

Kremkau, F. W., *Diagnostic Ultrasound*. W.B. Saunders Company, Philadelphia, 1993.

Lamb, G. D., "Tactile discrimination of textured surfaces: Psychophysical performance measurements in humans," *Journal of Physiology (London)*, vol. 338, pp. 551–565, 1983.

LaMotte, R. H. and Srinivasan, M. A., "Responses of cutaneous mechanoreceptors to the shape of objects applied to the primate fingerpad," *Acta Psychologica*, vol. 84, pp. 41–51, 1993.

Lanir, Y., "Skin mechanics," in *Handbook of Bioengineering*, ch. 11, pp. 11.1–11.25, McGraw-Hill, 1987.

Lederman, S. J. and Taylor, M. M., "Fingertip force, surface geometry, and the perception of roughness by active touch," *Perception & Psychophysics*, vol. 12, pp. 401–408, 1972.

Lemons, R. A. and Quate, C. F., "Acoustic microscopy," in *Physical Acoustics* (Mason, W. P. and Thurston, R. N., eds.), vol. 5, pp. 1–92, Academic Press, New York, 1979.

Lockhart, R. D., Hamilton, G. F., and Fyfe, F. W., *Anatomy of the Human Body*. J P Lippincott Co., Philadelphia, 1965.

Loewenstein, W. R. and Skalak, R., "Mechanical transmission in a pacinian corpuscle. An analysis and a theory," *J. Physiol*, vol. 182, pp. 346–378, 1966.

Loomis, J. M., "An investigation of tactile hyperacuity," *Sensory Processes*, vol. 3, pp. 289–302, 1979.

Loomis, J. M. and Lederman, S. J., "Tactual perception," in *Handbook of perception and human performance*, ch. 31, pp. 31.1–31.41, John Wiley & Sons, 1986.

Morgan, K., Dayton, P., Brandenburger, G., Kaul, S., Wei, K., and Ferrara, K., "Properties of contrast agents insonified at frequencies above 10 MHz," *Ultrasonics Symposium*, pp. 1127–1130, 1996.

Mountcastle, V. and Powell, T., "Central nervous mechanisms subserving position sense and kinesthesis," *Bulletin of the Johns Hopkins Hospital*, vol. 105, pp. 173–200, 1959.

Mountcastle, V., LaMotte, R., and Carli, G., "Detection thresholds for stimuli in humans and monkeys: Comparison with thresholds events in mechanoreceptive afferent nerve fibers innervating in the monkey hand," *J. Neurophysiol*, vol. 35, pp. 122–136, 1972.

O'Donnell, M., Skovoroda, A. R., Shapo, B. M., and Emelianov, S. Y., "Internal displacement and strain imaging using ultrasonic speckle tracking," *IEEE Transactions on Ultrasonics, Ferroelectrics and Frequency Control*, vol. 41, no. 3, pp. 314–325, 1994.

O'Rahilly, R., "Skin, hair, and nails," in *Anatomy: A Regional Study of the Human Structure* (Gardner, E. and O'Rahilly, D. G. R., eds.), W. B. Saunders and Co., 1969.

Passmann, C. and Ermert, H., "A 100 MHz ultrasound imaging system for dermatologic and ophthalmologic diagnostics," *IEEE Transactions on Ultrasonics, Ferroelectrics, and Frequency Control*, vol. 43, no. 4, pp. 545–553, 1996.

Phillips, J. R. and Johnson, K. O., "Tactile spatial resolution - II. Neural representation of bars, edges and gratings in monkey afferents," in *J. Neurophysiol* (Phillips and Johnson, 1981b), pp. 1192–1203.

Phillips, J. R. and Johnson, K. O., "Tactile spatial resolution - III. A continuum mechanics model of skin predicting mechanoreceptor responses to bars, edges and gratings," *J. Neurophysiol*, vol. 46, pp. 1204–1225, 1981b.

Raju, B. I., "Encoding and decoding of shape during tactile sensing," Master's thesis, Mech. Engg. Dept., MIT, February 1998.

Sherar, M. D. and Foster, F. S., "A 100 MHz PVDF ultrasound microscope with biological applications," in *Acoustical Imaging* (Kessler, L. W., ed.), pp. 511–520, Plenum Press, 1987b.

Sherar, M. D. and Foster, F. S., "The design and fabrication of high frequency poly(vinylidene flouride) transducer," *Ultrasonic Imaging*, vol. 11, pp. 75–94, 1989a.

Shung, K. K., Smith, M. B., and Tsui, B. M. W., *Principles of Medical Imaging*. Academic Press, Inc., New York, 1992.

Srinivasan, M. A., "Surface deflection of primate fingertip under line load," *J. Biomechanics*, vol. 22, no. 4, pp. 343–349, 1989.

Srinivasan, M. A. and LaMotte, R. H., "Tactual discrimination of softness," *J.Neurophysiol*, vol. 73, no. 1, pp. 88–101, 1995.

Srinivasan, M. A. and LaMotte, R. H., "Tactile discrimination of shape: Responses of slowly and rapidly adapting mechanoreceptive afferents to a step indented into the monkey fingerpad," *Journal of Neuroscience*, vol. 7, no. 6, pp. 1682–1697, 1987.

Talbot, W. H., Darian-Smith, I., Kornhuber, H. H., and Mountcastle, V. B., "The sense of flutter-vibration: Comparison of the human capacity with response patterns of mechanoreceptive afferents from the monkey hand," *J.Neuorphysiol*, vol. 31, pp. 301–334, 1968.

Thomine, J., "The skin of the hand," in *The Hand* (Tubiana, R., ed.), vol. 1, ch. 6, pp. 107–120, W. B. Saunders and Co., 1981.

Tregear, R. T., *Physical Functions of Skin*. Academic Press, New York, 1966.

Turnbull, D. H., Starkoski, B. G., Harasiewicz, K. A., Lockwood, G. R., and Foster, F. S., "Ultrasound backscatter microscope for skin imaging," *Ultrasonics Symposium*, pp. 985–988, 1993.

Verillo, R. T., Fraioli, A. J., and Smith, R. L., "Sensation magnitude of vibrotactile stimuli," *Perception & Psychophysics*, vol. 6, pp. 366–372, 1969.

Voss, K. J. and Srinivasan, M., "Investigation of the internal geometry and mechanics of the human fingertip, *in vivo*, using magnetic resonance imaging," *RLE TR-622, MIT*, 1998.

Wiersema, M. J., Reilly, C. R., Sanghvi, N. T., Hawes, R., Wiersema, L., and Aust, C., "25 Megahertz gastrointestinal ultrasonography," *Ultrasonics Symposium*, pp. 845–848, 1989.

Zhou, X. and Johnson, A., "Magnetic resonance microscopy," in *The Biomedical Engineering Handbook* (Bronzino, J., ed.), ch. 68, pp. 1119–1133, CRC Press and IEEE Press, 1995.